Negative Asymmetric Response of Pantropical Gross Primary Productivity to Precipitation Anomalies

Lei Fan, Guanyu Dong, Philippe Ciais, Xiangming Xiao, Jingfeng Xiao, Xiuzhi Chen, Yiqi Luo, Shuli Niu, Fei Jiang, Frédéric Frappart, et al.

Earth's Future

RESEARCH ARTICLE
10.1029/2024EF004760

Negative Asymmetric Response of Pantropical Gross Primary Productivity to Precipitation Anomalies

Lei Fan[1,2], Guanyu Dong[1,2], Philippe Ciais[3], Xiangming Xiao[4], Jingfeng Xiao[5], Xiuzhi Chen[6], Yiqi Luo[7], Shuli Niu[8], Fei Jiang[9], Frédéric Frappart[10], Jean-Pierre Wigneron[10], Xing Li[11], Tianxiang Cui[12], Li Pan[4], and Rasmus Fensholt[13]

[1]Chongqing Jinfo Mountain Karst Ecosystem National Observation and Research Station, School of Geographical Sciences, Southwest University, Chongqing, China, [2]Chongqing Engineering Research Center for Remote Sensing Big Data Application, School of Geographical Sciences, Southwest University, Chongqing, China, [3]Laboratoire des Sciences du Climat et de l'Environnement, CEA-CNRS-UVSQ, Université Paris Saclay, Gif-Sur-Yvette, France, [4]Department of Microbiology and Plant Biology, Center for Earth Observation and Modeling, University of Oklahoma, Norman, OK, USA, [5]Earth Systems Research Center, Institute for the Study of Earth, Oceans, and Space, University of New Hampshire, Durham, NH, USA, [6]School of Atmospheric Sciences, Sun Yat-Sen University, Zhuhai, China, [7]Department of Microbiology and Plant Biology, University of Oklahoma, Norman, OK, USA, [8]Key Laboratory of Ecosystem Network Observation and Modeling, Institute of Geographic Sciences and Natural Resources Research, Chinese Academy of Sciences, Beijing, China, [9]International Institute for Earth System Science, Nanjing University, Nanjing, China, [10]INRAE, Université de Bordeaux, Bordeaux, France, [11]Research Institute of Agriculture and Life Sciences, Seoul National University, Seoul, South Korea, [12]Co-Innovation Center for Sustainable Forestry in Southern China, Nanjing Forestry University, Nanjing, China, [13]Department of Geosciences and Natural Resource Management, University of Copenhagen, Copenhagen, Denmark

Abstract The carbon sink in pantropical biomes play a crucial role in modulating the inter-annual variations of global terrestrial carbon balance and is threatened by extreme climate events. However, it has not been carefully examined whether an increase in tropical gross primary productivity (GPP) can compensate the decrease during precipitation anomalies. Using the asymmetry index (AI) and multiple GPP products, we assessed responses of pantropical GPP to precipitation anomalies during 2001–2022. Positive AI indicates that GPP increases are greater than GPP decreases during precipitation anomalies, and vice versa. Our results showed an average negative pantropical GPP asymmetry, that is, GPP decreases exceeded the GPP increases during precipitation anomalies. In addition, a positive AI was found in tropical hyper-arid and arid regions, which is opposite to the negative AI observed in tropical semi-arid, sub-humid, and humid regions. This suggest that tropical GPP asymmetry changes from positive to negative as the moisture increases. Notably, a significant decreasing trend of negative AI was observed over the entire tropical region, indicating that the negative effect of inter-annual precipitation variations on pantropical vegetation productivity has enhanced. Considering the model predicted increasing climate variability and extremes, the negative impact of precipitation variability on tropical carbon cycle may continue to intensify. Lastly, the divergence in AI estimates among multiple GPP products highlight the need to further improve our understanding of the response of tropical carbon cycle to climate changes, especially for the tropical humid regions.

Plain Language Summary Tropical biomes play an essential role in controlling the global carbon balance but has been threatened by extreme climate events recently. Whether the increase in tropical GPP can compensate the GPP decrease during precipitation anomalies is still poorly known. In this study, we found an average negative asymmetric GPP response to precipitation anomalies over the entire tropics during 2001–2022, that is, GPP decreases exceeded the GPP increases during precipitation anomalies. Meanwhile, we found that the tropical GPP was shifted from positive asymmetry to negative asymmetry as the moisture increases. Besides, a significantly decreasing trend of GPP asymmetry was observed over the study period, suggesting that the negative effect of inter-annual precipitation variations on pantropical GPP has intensified.

Key Points:

- We find the tropical GPP shows a negative asymmetric response to precipitation anomalies over the past two decades
- An overall decreasing trend of the GPP asymmetry was observed over the entire tropical region
- Anisohydric biomes have a stronger positive asymmetric response of GPP to precipitation anomalies than isohydric biomes

Supporting Information:

Supporting Information may be found in the online version of this article.

Correspondence to:

G. Dong,
dgy199909@email.swu.edu.cn

Citation:

Fan, L., Dong, G., Ciais, P., Xiao, X., Xiao, J., Chen, X., et al. (2024). Negative asymmetric response of pantropical gross primary productivity to precipitation anomalies. *Earth's Future*, *12*, e2024EF004760. https://doi.org/10.1029/2024EF004760

Received 5 APR 2024
Accepted 11 SEP 2024

Author Contributions:

Conceptualization: Lei Fan, Guanyu Dong
Data curation: Guanyu Dong
Formal analysis: Guanyu Dong
Funding acquisition: Lei Fan
Methodology: Guanyu Dong
Supervision: Lei Fan
Visualization: Guanyu Dong
Writing – original draft: Lei Fan, Guanyu Dong
Writing – review & editing: Lei Fan, Guanyu Dong, Philippe Ciais, Xiangming Xiao, Jingfeng Xiao, Xiuzhi Chen, Yiqi Luo, Shuli Niu, Fei Jiang, Frédéric Frappart, Jean-Pierre Wigneron, Xing Li, Tianxiang Cui, Rasmus Fensholt

1. Introduction

Tropical biomes hold the Earth's largest carbon pool (Chen et al., 2017; Pan et al., 2011; Wigneron et al., 2024), especially for tropical forests accounting for approximately half of the global gross primary production (GPP) (Wang et al., 2024). Slight fluctuations of tropical forest growth and mortality could profoundly impact the global

Table 1
Summary of Satellite Model-Based GPP Products

Name	GPP category	Spatial resolution	Temporal resolution	Period
VPM	LUE	0.05°	monthly	2001–2022
BEPS	Process	0.072727°	daily	2001–2019
MODIS	LUE	500 m	8-day	2001–2022
FLUXCOM	ML	0.5°	monthly	2001–2017
Prentice	LUE	0.5°	daily	2001–2016
BESS	Process	0.25°	monthly	2001–2019

Note. LUE, light use efficiency; ML, machine learning; Process, process-based model.

carbon balance, and even exacerbate the rise in atmospheric CO_2 concentrations (Espirito-Santo et al., 2014). Extreme climates pose threats to the pantropical terrestrial ecosystems (Niu et al., 2014; Wigneron et al., 2020). Major droughts and fires occurred in tropical regions in 1982, 1997–1998, 2005, 2010 and 2015–2016, and have markedly decreased vegetation productivity and increased vegetation mortality (Yue et al., 2017). In particular, the 2015–2016 El Niño event induced unprecedented high temperatures and rainfall anomalies in pantropical regions (Jimenez-Munoz et al., 2016), leading to pantropical regions acted as a carbon source during this period (Liu et al., 2017; Yue et al., 2017). Despite the return to wetter conditions during La Niña years could stimulate the recovery of tropical vegetation production (Yang et al., 2022), the post-drought legacy impacts on plant growth may still result in persistent declines in tropical vegetation productivity and biomass, countering the expected productivity recovery from increased precipitation (Wigneron et al., 2020). Whether the pantropical GPP increases can compensate for the GPP decreases during the precipitation anomalies is currently poorly known, and remains to be studied.

Global terrestrial ecosystem productivity has shown an asymmetric response to wet and dry anomalies (Haverd et al., 2017; Wang et al., 2022), but inconsistent results regarding pantropical GPP asymmetry have been reported among different studies, likely owing to the differences in data sources, the complexity of pantropical ecosystems, and the challenges in accurately measuring pantropical GPP. For example, by using up-scaled GPP estimates based on eddy covariance (EC) data, a previous study Haverd et al. (2017) reported that tropical GPP exhibited a positive asymmetry for the past 30 years in response to precipitation anomalies. In contrast, negative asymmetries with varying magnitude were observed over the pantropical regions (Haverd et al., 2017; Zscheischler et al., 2014a, 2014b), when using multiple GPP data sets simulated by vegetation models. These discrepancies call for further studies on the asymmetric pantropical GPP responses to precipitation anomalies.

Previous studies explored possible drivers for GPP asymmetries, and found precipitation to be the dominant variable controlling the spatiotemporal changes in GPP asymmetry (Ahlstrom et al., 2015), and root-zone soil moisture as well as aridity have been reported as important indicators for assessing the dynamic of water availability (Stocker et al., 2019). Moreover, within the era of global warming, plants can develop different water regulation strategies (isohydric and anisohydric plant functional traits) to improve resistance and resilience to drought (Konings & Gentine, 2017; McDowell et al., 2008), which may profoundly influence the GPP asymmetry.

Here, we utilized multiple GPP products to investigate asymmetric GPP responses to precipitation anomalies in the tropics (here defined as 24°N–24°S, including tropical America, Africa, Asia and Australia) over 2001–2022. Our aims are to: (a) examine the spatial-temporal patterns of tropical GPP asymmetry, (b) assess the tropical GPP asymmetry for separate biomes and aridity zones, and (c) analyze the influence of multiple environmental factors (average climate state and soil properties) and plant ecophysiological characteristics (isohydricity, canopy height, and rooting depth) on the tropical GPP asymmetry.

2. Materials

2.1. GPP Data Sets

1. *Satellite model-based GPP*. Multiple GPP data sets were utilized to compute tropical GPP asymmetry (Table 1), including the vegetation photosynthesis model (VPM) GPP (Zhang et al., 2017), boreal ecosystem productivity simulator (BEPS) GPP (Chen et al., 2019), moderate resolution imaging spectroradiometer (MODIS) GPP (Running et al., 2015), FLUXCOM GPP (Jung et al., 2019), Prentice GPP (Stocker et al., 2020), and breathing earth system simulator (BESS) GPP (Jiang & Ryu, 2016). Considering that the raw spatial resolution is 0.25° for multiple environmental variables (see Section 2.2 for details of environmental variables), these satellite model-based GPP used here were aggregated to 0.25° spatial resolution, and averaged for each hydrological year (October–following September):

The GPP product from the VPM model (GPP_{VPM}) was generated by an advanced light use efficiency (LUE) algorithm, using satellite vegetation data (i.e., MODIS enhanced vegetation index (EVI) and land surface water index (LSWI)) and national centers for environmental prediction (NCEP) climate data (Zhang et al., 2017). The LUE algorithm has been widely used to the global GPP estimates (Zhang et al., 2017), due to its simplicity and the relatively long time period of data availability. However, the bias in the simulation of the relationship between water stress and LUE may existed in some LUE-based models (Heinsch et al., 2006), leading to the uncertainties of GPP estimates. Here, monthly GPP_{VPM} data at 0.05° for the hydrological year of 2001–2022 were selected.

In contrast to the LUE models, the process-based BEPS model additionally considers the CO_2 concentration and nutrient deposition effects on GPP, driven by leaf area index (LAI), clumping index, land cover type, climate and soil data (Chen et al., 2019). For the GPP estimates, BEPS model employs a leaf-level biochemical model with a two-leaf (i.e., sunlit and shaded leaves) upscaling scheme from leaf to canopy, combined using the Farquhar model (Chen et al., 1999). Daily GPP_{BEPS} data (spatial resolution, 0.072727°) for the hydrological year of 2001–2019 were used.

The MODIS MOD17A2H V6 GPP product (GPP_{MODIS}) is calculated based on a MOD17 algorithm, using a LUE approach (Running et al., 2015). However, the MOD17 algorithm assumes that the LUE for each vegetation type remains constant (Running et al., 2015), and optical remote sensing measurements are susceptible to atmospheric conditions, especially in the tropics where cloud cover and aerosol effects occurred frequently (Zeng, Hao, et al., 2022), potentially affecting the accuracy of GPP estimates. Considering the relatively long time period of GPP_{MODIS}, 8-day GPP_{MODIS} data (spatial resolution, 500 m) for the hydrological years of 2001–2022 were used.

The FLUXCOM GPP product ($GPP_{FLUXCOM}$) is generated by upscaling the EC fluxes of FLUXNET observations to global scale based on machine learning (Jung et al., 2019). It should be noted that the uncertainty of FLXCOM GPP is higher in the tropics than in other regions, owing to the complexity of tropical ecosystems and limited FLUXNET sites in the tropics (Jung et al., 2020). The FLUXCOM includes various GPP subsets driven by diverse meteorological data sets. Here, the monthly FLUXCOM GPP forced by the CRU-JRA data (spatial resolution, 0.5°) over the period 2001–2017 was selected, as it covered the longest time period.

The Prentice GPP, being a LUE-model based GPP product ($GPP_{Prentice}$), is forced by the site-scale carbon and water flux measurements (Stocker et al., 2020). Daily Prentice GPP (spatial resolution, 0.5°) from 2001 to 2016 was used.

The BESS V2 GPP (GPP_{BESS}) is derived by a process-based model that coherently integrated land-atmosphere physical and biochemical processes (Jiang & Ryu, 2016). Monthly BESS GPP (spatial resolution, 0.25°) for the hydrological years of 2001–2019 were used here.

(2) *Site GPP*. Two ground-based site level GPP data sets (GPP_{EC}) were selected to confirm the pantropical GPP asymmetry based on the satellite observations, including FLUXNET2015 (Pastorello et al., 2020) and Terrestrial Ecosystem Research Network (TERN) data set (Karan et al., 2016).

For the FLUXNET 2015 data set, the monthly GPP reference data derived by a day-time flux partitioning method were selected. For the TERN data set, the monthly GPP data generated from artificial neural networks were selected, because some TERN sites do not provide GPP data produced from the day-time approach.

Since there are a limited number of EC sites providing flux measurements in tropics, only eight EC sites having an observation period longer than eight hydrological years were available for this study (Table 2), consisting of four

Table 2
Summary of the GPP Flux Sites

Site ID	Data set	Latitude	Longitude	Vegetation type	Period
AU-ASM	TERN	−22.2828	133.2493	SAV	2011–2022
AU-CB	TERN	−16.2382	145.4272	EBF	2010–2021
AU-CT	TERN	−16.1032	145.4470	EBF	2011–2018
AU-How	FLUXNET2015	−12.4943	131.1523	WSA	2001–2013
AU-Stp	TERN	−17.1507	133.3502	GRA	2009–2020
AU-TTE	TERN	−22.2870	133.6400	GRA	2013–2020
BR-Sa1	FLUXNET2015	−2.8567	−54.9589	EBF	2003–2010
GF-Guy	FLUXNET2015	5.2788	−52.9249	EBF	2005–2013

Note. SAV, savannas; GRA, grasslands; WSA, woody savannas; EBF, evergreen broadleaf forests.

evergreen broadleaf forest (EBF) sites, two grassland (GRA) sites, one savanna (SAV) site, and one woody savanna (WSA) site. We further merged WSA into SAV and renamed EBF as forests. Consequently, the vegetation types of the EC sites were stratified into three classes: forests, savannas, and grasslands.

2.2. Environmental Variables

All the environmental variables were also aggregated to hydrological annual composites at 0.25° resolution, in order to ensure a uniform spatial resolution.

1. *Precipitation*, provided by Climate Hazards Group InfraRed Precipitation with Station Data (CHIRPS) data set (Funk et al., 2015). CHIRPS is a long-term global precipitation data set that is suited for the monitoring of drought events accurately (Funk et al., 2015), providing daily and pentad precipitation data at 0.05° spatial resolution. Here, daily CHIRPS precipitation data during 2001–2022 were selected.
2. *Root-zone soil moisture (RZSM)*, derived from the fifth generation of the land component of the ECMWF reanalysis (ERA5-Land) data set (Hersbach, 2019). ERA5-Land provides monthly averaged soil moisture (SM) at a 0.25° spatial resolution. In this present study, monthly ERA5-Land SM below 100 cm depth were selected to calculate the RZSM (in units of $m^3\ m^{-3}$) during 2001–2022, using a weighted average method (Fan et al., 2024; Gonzalez-Zamora et al., 2016; Martínez-Fernández et al., 2019) as follows:

$$\mathrm{RZSM} = 0.07 \times \theta_{7\mathrm{cm}} + 0.21 \times \theta_{28\mathrm{cm}} + 0.72 \times \theta_{100\mathrm{cm}} \quad (1)$$

   where $\theta_{7\mathrm{cm}}$, $\theta_{28\mathrm{cm}}$, and $\theta_{100\mathrm{cm}}$ represent the 0–7, 7–28 and 28–100 SM, respectively.
3. *Vapor pressure deficit (VPD)*, provided by the TerraClimate data set (Abatzoglou et al., 2018). Monthly VPD data (kPa) for 2001–2022 with 1/24° resolution were selected.
4. *Photosynthetically Active Radiation (PAR)*, derived from the ERA5-Land data set (Hersbach, 2019). ERA5-Land provides monthly downward shortwave radiation at the spatial resolution of 0.25°. We converted the original unit ($J\ m^{-2}$) to the $W\ m^{-2}$ through dividing by the accumulation period. Monthly ERA5-Land downward shortwave radiation from 2001 to 2022 were converted to PAR by multiplying a factor of 0.5 (Chen et al., 1999).
5. *Air temperature*, obtained from ERA5-Land data set (Hersbach, 2019). The ERA5-Land provides above-ground air temperature at 2 m. We converted an original unit (K) into degrees centigrade (°C). Monthly ERA5-Land air temperature for 2001–2022 were selected.

2.3. Ancillary Data Sets

All ancillary data sets were aggregated to a 0.25° resolution for ensuring a uniform spatial resolution across the whole study.

1. *Land cover map*, derived from the MODIS MCD12Q1 product at 500-m spatial resolution during 2001–2020 (Friedl et al., 2019). The MCD12Q1 land cover map with the International Geosphere-Biosphere Program

(IGBP) land cover classification was used to identify the land cover type for each pixel. Pixels dominated by croplands and non-vegetated land cover types were excluded. We further merged evergreen needleleaf forests, evergreen broadleaf forests, deciduous needleleaf forests, deciduous broadleaf forests, and mixed forests into forests. Closed shrublands and open shrublands were merged into shrublands. Woody savannas were merged into savannas. All pixels where land cover change has occurred during 2001–2020 were excluded from further analysis. Accordingly, tropical vegetation is characterized by four land cover types (Figure S1a in Supporting Information S1), namely, forests (covering 29.21% of the tropical region), shrublands (covering 8.69% of the tropical region), savannas (covering 29.12% of the tropical region), and grasslands (covering 32.98% of the tropical region).

2. *Forest cover loss*, defined as a stand-replacement disturbance or a change from a forest to a non-forest state. We calculated forest loss rates at 0.25° spatial resolution by Hansen forest cover loss map (Hansen et al., 2013), namely, the percentage of forest cover loss areas within each 0.25° pixel during the period 2001–2022. All pixels with more than 5% forest loss rates were defined as forest cover loss regions and were excluded from further analysis.
3. *Forest degradation*, defined as a disturbance in the forest canopy that is visible from space over a short time period, leading to biodiversity and carbon losses. We calculated forest degradation rates at 0.25° spatial resolution by Vancutsem forest degradation map (Vancutsem et al., 2021), namely, the percentage of forest degradation areas within each 0.25° pixel. All pixels with more than 5% forest degradation rates were defined as forest-degradation regions and were excluded from further analysis.
4. *Aridity index*, is provided by Global Aridity Index V3.0 data set (Zomer et al., 2022) at the spatial resolution of 30 arc-seconds, is computed by the ratio of precipitation to potential evapotranspiration from WorldClim V2.1 data set (Zomer et al., 2022), which can be used to indicate the moisture of the pantropical regions. Accordingly, tropical drylands are defined by aridity index <0.65 and include four sub-types (Berg & McColl, 2021): hyper-arid (aridity index < 0.05), arid ($0.05 \leq$ aridity index < 0.2), semi-arid ($0.2 \leq$ aridity index < 0.5), and sub-humid regions ($0.5 \leq$ aridity index < 0.65). The tropical humid regions are defined by aridity index ≥ 0.65 (Figure S1b in Supporting Information S1).
5. *Isohydricity data*, estimated using Ku-Band backscatter data (including both V- and H-polarizations) from the active microwave satellite QuikSCAT (Li et al., 2017). Plants are characterized by different water regulation strategies through stomatal and xylem regulation, spanning from being strictly isohydric to highly anisohydric (McDowell et al., 2008). Biomes dominated by isohydric plants are known to develop a conservative phenological strategy through stomatal closure and leaf drop to reduce water losses and avoid hydraulic failure (leading to a relative stability of leaf water potential) during the drought period (McDowell et al., 2008). Biomes dominated by more anisohydric plants, by contrast, could keep their stomata relatively open and effectively allow leaf water potential to decrease as SM declines during moisture deficit states (McDowell et al., 2008). In accordance with the static isohydricity data, higher values indicate more anisohydric functioning, and lower values indicate more isohydric functioning (Li et al., 2017). Here, only the V-polarization isohydricity data at a 0.05° spatial resolution were selected, as two polarizations (H and V) of QuickSCAT exhibit similar spatial patterns of isohydry/anisohydry estimates (Li et al., 2017).
6. *Maximum rooting depth*, provided from the European Commission EartH2Observe and estimated from an inverse model (Fan et al., 2017). Maximum rooting depth at a 30″ (~1-km) spatial resolution was selected.
7. *Canopy height*, derived from Global 1 km Forest Canopy Height database (Simard et al., 2011). The canopy height product was calculated using the 2005 GLAS LiDAR measurements, combining the tree cover and meteorological data.
8. *Soil organic carbon (SOC) and soil sand fraction*, derived from Harmonized World Soil Database (HWSD) version 1.2 (Wieder, 2014). Here the 0.05° spatial resolution SOC and soil sand fraction from the depth of 0–30 cm were selected.

3. Methods

3.1. Asymmetry Index

An asymmetry index (AI) was applied to assess asymmetric GPP responses to precipitation anomalies in the tropics. For each pixel, we filtered out linear trends from the time series of GPP and precipitation to avoid spurious GPP-precipitation correlations due to long-term trends. On this basis, we computed the standardized anomaly

(SA) of detrended GPP and precipitation, for better understanding the relative difference in the GPP asymmetry across biomes and aridity gradients:

$$X_{\mathrm{SA},i} = \frac{X_i - \overline{X}}{\sigma} \tag{2}$$

where X is the detrended GPP or precipitation, $X_{\mathrm{SA},i}$ represents the SA value of X in the year i. $\overline{X}$ and σ indicate the long-term mean and standard deviation value of X over the study period, respectively. We partitioned the precipitation anomalies into wet and dry anomalies, and defined the wet anomalies (or wet years) and the dry anomalies (or dry years) as the years with $\mathrm{precipitation_{SA}}$ value > 1 and $\mathrm{precipitation_{SA}}$ value < -1, respectively (Zaveri et al., 2020).

We further calculated the tropical GPP responses during the wet and dry anomalies, as follows:

$$\mathrm{GPP}_W = \overline{\mathrm{GPP}_{\mathrm{SA,wet}}} \tag{3}$$

$$\mathrm{GPP}_D = \overline{\mathrm{GPP}_{\mathrm{SA,dry}}} \tag{4}$$

$$\mathrm{AI} = \mathrm{GPP}_W + \mathrm{GPP}_D \tag{5}$$

where GPP_W and GPP_D represent the response of pantropical GPP to wet and dry anomalies, respectively. Moreover, AI is calculated by the sum of GPP_W and GPP_D. AI > 0 indicates a positive GPP asymmetry, indicating that GPP increases are higher than GPP decreases during the precipitation anomalies, and vice versa for AI < 0. By using this method, we also calculated the $\mathrm{precipitation_W}$ and $\mathrm{precipitation_D}$ values to represent the intensities of wet and dry anomalies, and calculated the AI values of precipitation to represent the asymmetric distribution of wet and dry anomalies (Figure S2 in Supporting Information S1). Generally, our results showed that the spatial distribution of wet anomalies matched with the spatial distribution of dry anomalies (Figures S2a and S2b in Supporting Information S1), and that the AI of precipitation anomalies is close to neutral (Figure S2c in Supporting Information S1). Thus, this method ensures that the GPP asymmetry is caused by the intrinsic asymmetric sensitivities of GPP to the precipitation anomalies, rather than the asymmetry caused by the asymmetric distribution of precipitation anomalies over the tropics (Zhao et al., 2022).

3.2. Analysis of GPP Asymmetry

One-way analysis of variance (ANOVA) was used to examine the statistical differences ($P < 0.05$) in GPP asymmetry for each biome and aridity zone (Sun et al., 2023). To analyze how the magnitude of precipitation anomalies affects the GPP asymmetry, we varied the magnitude of precipitation anomalies used for analysis by changing the $\mathrm{precipitation_{SA}}$ thresholds that define the wet and dry anomalies (ranging from ±1 to ±2) (Famiglietti et al., 2021). We calculated the AI value for each flux site ($\mathrm{AI_{EC}}$) based on the available time periods of the flux sites and computed Pearson's correlation coefficient ($P < 0.05$) between $\mathrm{AI_{EC}}$ and the AI values of the corresponding remote sensing pixels, in order to compare biome-scale and site-scale AI values in the tropics.

Based on previous studies (Al-Yaari et al., 2020; Chang et al., 2023), we selected a 11-year temporal moving window to compute the running mean of the AI value, and used a linear regression method to analyze the trends of tropical GPP asymmetry. For details, we computed the SA values of detrended GPP and precipitation over the entire period of 2001–2022, to ensure that the mean GPP and variance of GPP in each temporal moving window remained consistent. Then we used the corresponding SA values of detrended GPP and precipitation in each window to generate the time series of AI, which was used to calculate the trends of tropical GPP asymmetry. In addition, we selected different window lengths (9, 11, 13, 15 years) to test the robustness of the tropical GPP asymmetry trends (see Section 4.2). Here, GPP asymmetry trends with $P < 0.1$ were regarded as statistically significant. Moreover, all variables used to analyze the influencing factors on tropical GPP asymmetry were unified as static data by calculating multiyear average values.

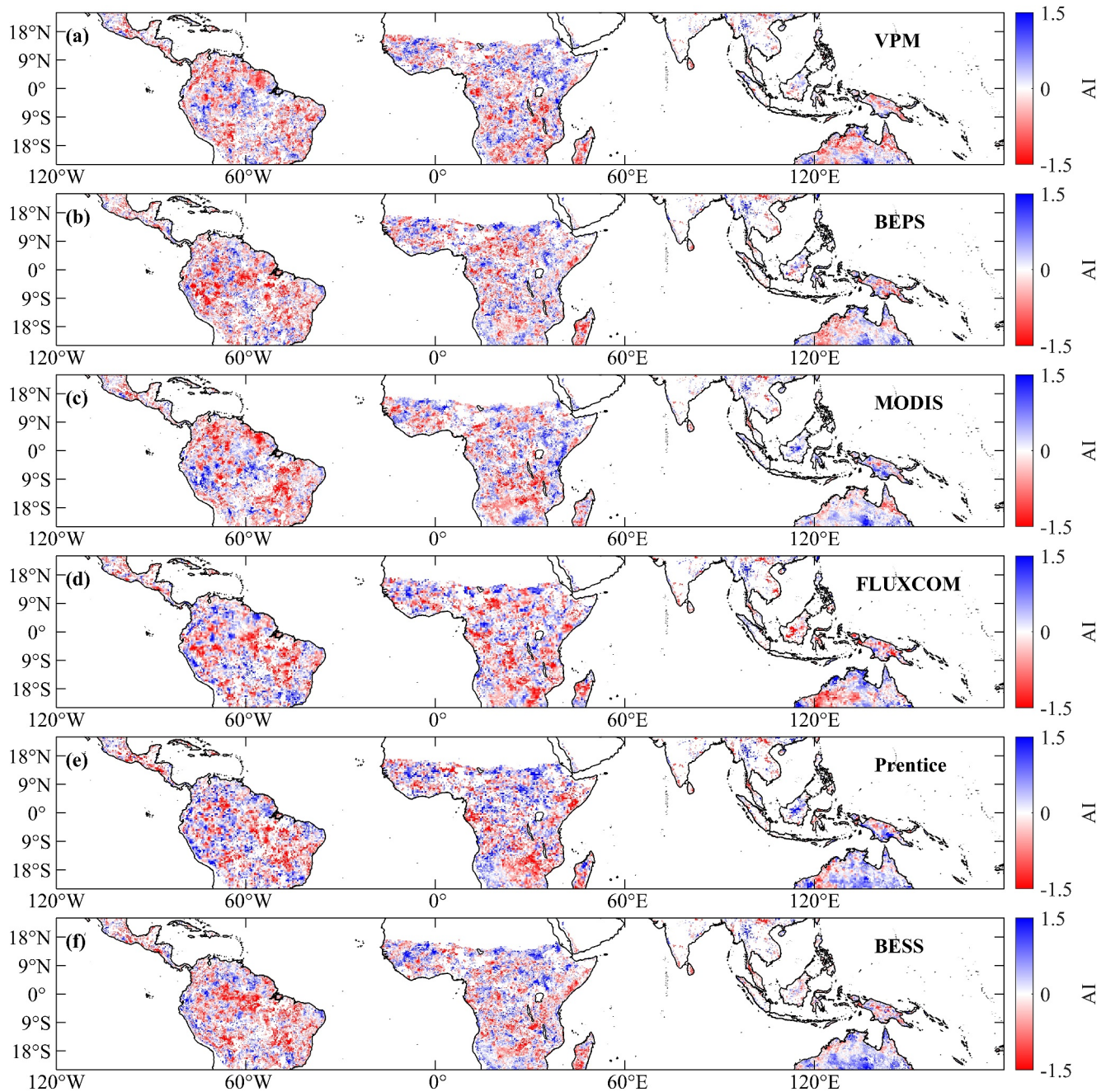

Figure 1. Spatial patterns of the GPP asymmetry in the tropics during 2001–2022: (a) AI_{VPM}; (b) AI_{BEPS}; (c) AI_{MODIS}; (d) $AI_{FLUXCOM}$; (e) $AI_{Prentice}$; (f) AI_{BESS}.

4. Results

4.1. Spatial Patterns of Tropical GPP Asymmetry

Across the different GPP products, the spatial pattern of the tropical GPP asymmetry was generally consistent in drylands but different in humid regions (Figure 1), with negative AI values mainly observed in most parts of tropical America, central and southern tropical Africa, Madagascar, New Guinea, and northern Australia. By contrast, positive AI values were mainly located in southeastern Australia.

During 2001–2022, the response of GPP to precipitation anomalies exhibited an overall negative asymmetry over the entire pantropical regions (−0.115 for $AI_{FLUXCOM}$, −0.104 for AI_{BEPS}, −0.081 for AI_{VPM}, −0.072 for

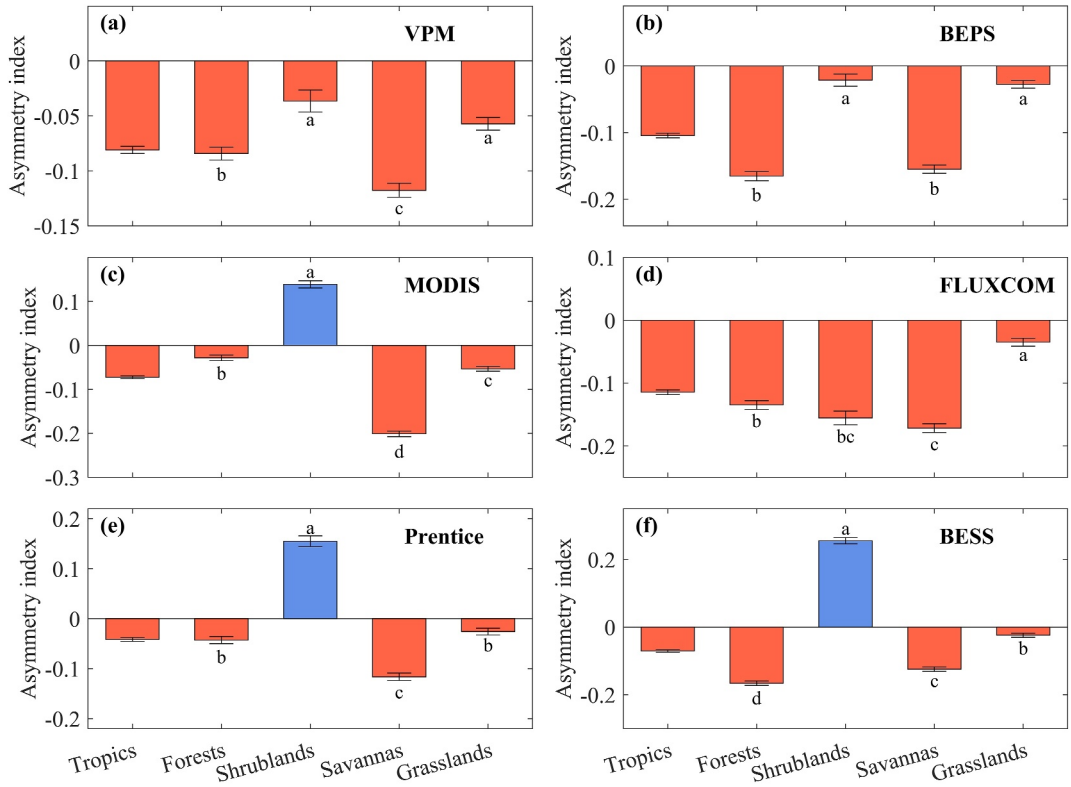

Figure 2. Bar plot of average asymmetry index (AI) values for each biome as well as for the pantropical area: (a) AI_{VPM}; (b) AI_{BEPS}; (c) AI_{MODIS}; (d) $AI_{FLUXCOM}$; (e) $AI_{Prentice}$; (f) AI_{BESS}. The error bars show the standard error. Different letters show significant differences ($P < 0.05$) in AI values among biomes.

AI_{MODIS}, −0.071 for AI_{BESS}, −0.041 for $AI_{Prentice}$) (Figure 2). This suggests that the GPP decreases generally exceed the GPP increases in response to the precipitation anomalies. The AI values of GPP were consistently negative for forests, savannas, and grasslands, with savannas displaying the strongest negative AI value for most GPP products (Figure 2). Specifically, in the case of GPP_{VPM}, the negative asymmetry in grasslands ($AI_{VPM} = -0.057$) is caused by a larger GPP decrease during dry anomalies ($GPP_D = -0.387$) as compared to the GPP increases during wet anomalies ($GPP_W = 0.33$) (Figures S3a, S3b and S4a in Supporting Information S1). In contrast, a negative GPP asymmetry in forests ($AI_{VPM} = -0.084$) is due to a larger GPP decrease during wet anomalies ($GPP_W = -0.486$) than GPP increases during dry anomalies ($GPP_D = 0.402$) (Figures S3a, S3b and S4a in Supporting Information S1). For savannas, GPP decreased in both wet and dry anomalies ($GPP_W = -0.104$, $GPP_D = -0.014$), leading to the strongest negative asymmetry in savannas ($AI_{VPM} = -0.118$) (Figures S3a, S3b and S4a in Supporting Information S1). However, different AI results from GPP products were found in shrublands, as indicated by the AI_{VPM} (−0.036), AI_{BEPS} (−0.021), and $AI_{FLUXCOM}$ (−0.156) showing negative values, while the AI_{MODIS} (0.139), $AI_{Prentice}$ (0.155), and AI_{BESS} (0.256) show positive values (Figure 2).

The positive and negative asymmetry found at the biome-level could be observed at site scale, using the FLUXNET2015 and TERN GPP data sets (Figure 3). The AI values of EC-based GPP varied across tropical EC sites, ranging from a minimum value of −0.584 at GF-Guy to a maximum value of 0.924 at BR-Sa1 for the forest sites, from a minimum value of −0.083 at AU-How to a maximum value of −0.024 at AU-ASM for the savanna sites, and from a minimum value of −0.284 at AU-Stp to a maximum value of 1.055 at AU-TTE for the grassland sites (Figure 3a). The highest correlation between satellite model-based AI values and ground-based AI values was found for GPP_{VPM} ($R = 0.88$), followed by GPP_{MODIS} ($R = 0.8$), GPP_{BESS} ($R = 0.07$), while low or even negative correlation values were found for the other products: $GPP_{Prentice}$ ($R = -0.04$), GPP_{BEPS} ($R = -0.63$), and $GPP_{FLUXCOM}$ ($R = -0.78$). Consequently, given the high correlation between AI_{EC} and AI_{VPM}, and the longest period of data availability for GPP_{VPM}, the following analysis was mainly based on the AI_{VPM} results.

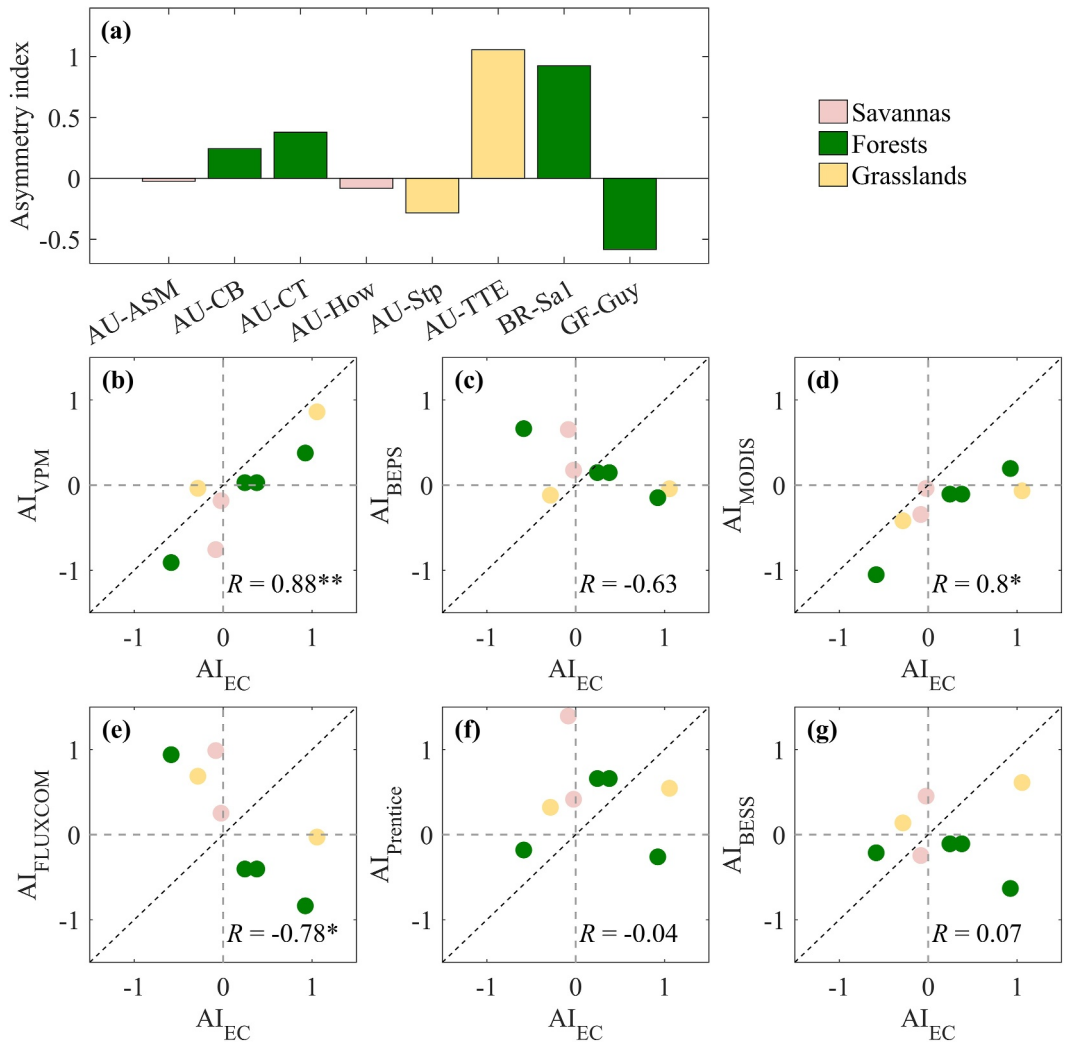

Figure 3. Asymmetric response of GPP to precipitation anomalies at site scale using FLUXNET2015 and TERN data set. (a) The asymmetry index (AI) value for each site. The relationships between AI_{EC} and AI_{VPM}, AI_{BEPS}, AI_{MODIS}, $AI_{FLUXCOM}$, $AI_{Prentice}$, and AI_{BESS} were shown in (b–g). The AI value for each site is calculated based on the time period of the flux sites. *R* indicates Pearson's correlation coefficient. * indicates $P < 0.05$ and ** indicates $P < 0.01$.

Additionally, the GPP asymmetry differed in sign across the aridity zones (Figure 4). Most positive AI values were found in hyper-arid regions, followed by arid, semi-arid, sub-humid, and humid regions. The strongest negative values of asymmetry were observed in tropical humid regions as the GPP decreases cannot be compensated by the GPP increases during precipitation anomalies (Figures S3 and S4 in Supporting Information S1). Furthermore, by modifying the $precipitation_{SA}$ thresholds used to identify precipitation anomalies, we found that the negative AI values decreased with a higher $precipitation_{SA}$ threshold (Figure S5 in Supporting Information S1), indicating that the negative GPP asymmetry over the tropics is robust over a wide range of the considered $precipitation_{SA}$ threshold, and that an increase in precipitation anomalies can have a negative impact on pantropical GPP asymmetry.

Overall, these results suggest that the pantropical regions generally showed a negative asymmetry in response of GPP to precipitation anomalies during 2001–2022. Also, the sign of the asymmetry varied across biomes and arid zones, with hyper-arid and arid biomes tending to exhibit positive asymmetry relative to the other biomes.

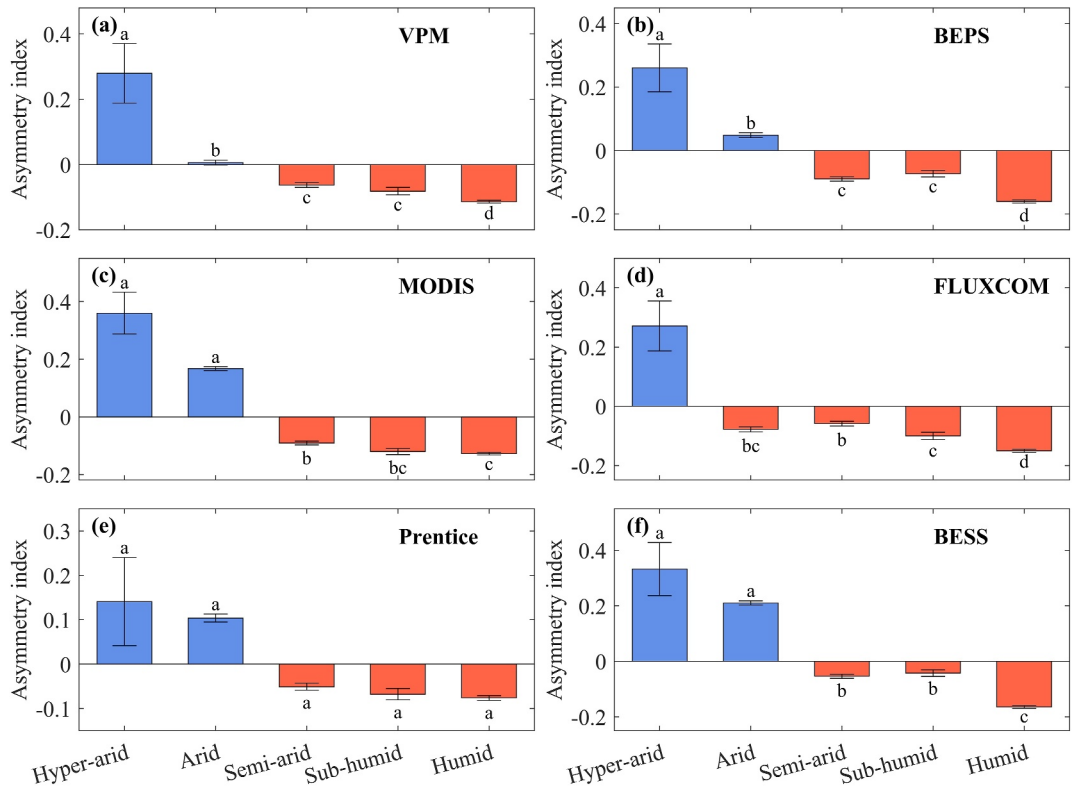

Figure 4. Bar plot of the average asymmetry index (AI) values for each aridity zone: (a) AI_{VPM}; (b) AI_{BEPS}; (c) AI_{MODIS}; (d) $AI_{FLUXCOM}$; (e) $AI_{Prentice}$; (f) AI_{BESS}. The error bars show the standard error. Different letters show significant differences ($P < 0.05$) in AI values among the aridity zones.

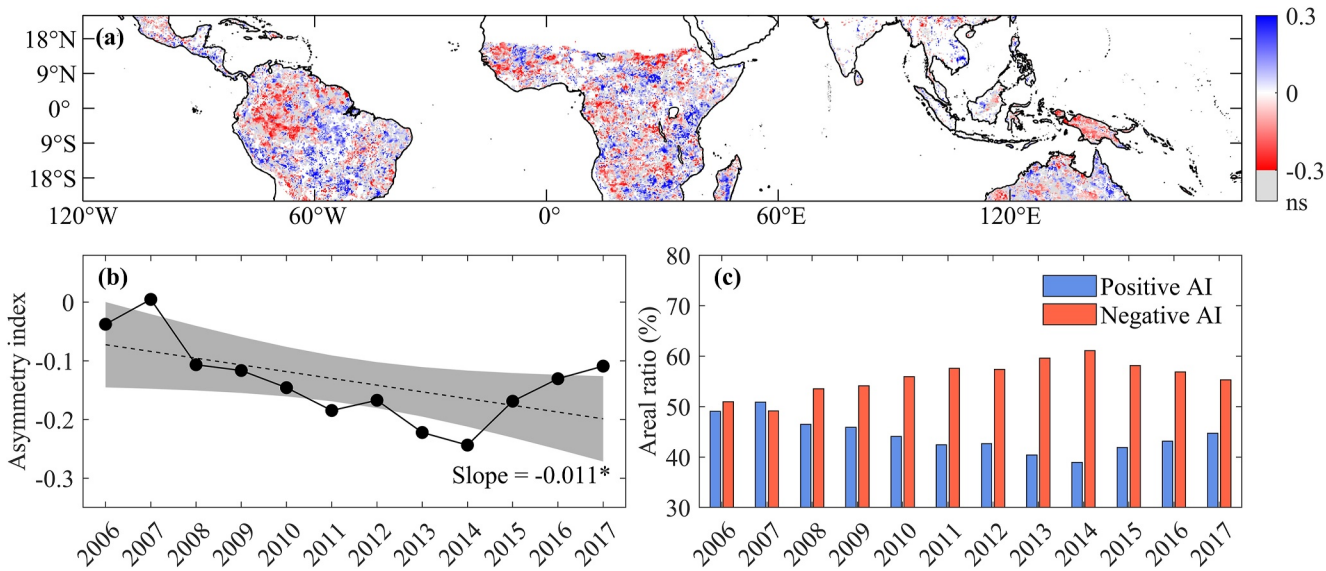

Figure 5. Trends in the asymmetry index (AI) of GPP in the tropics during 2001–2022 from GPP_{VPM}, calculated using a 11-year moving window. (a) Spatial pattern of the AI trends (linear trend; $P < 0.1$) in the tropics. Gray pixels correspond to areas where no significant trends were identified. (b) Trends of the average AI in the tropics. The shaded areas represent the 95% confidence interval. (c) Areal ratios of positive and negative AI value during 2001–2022.

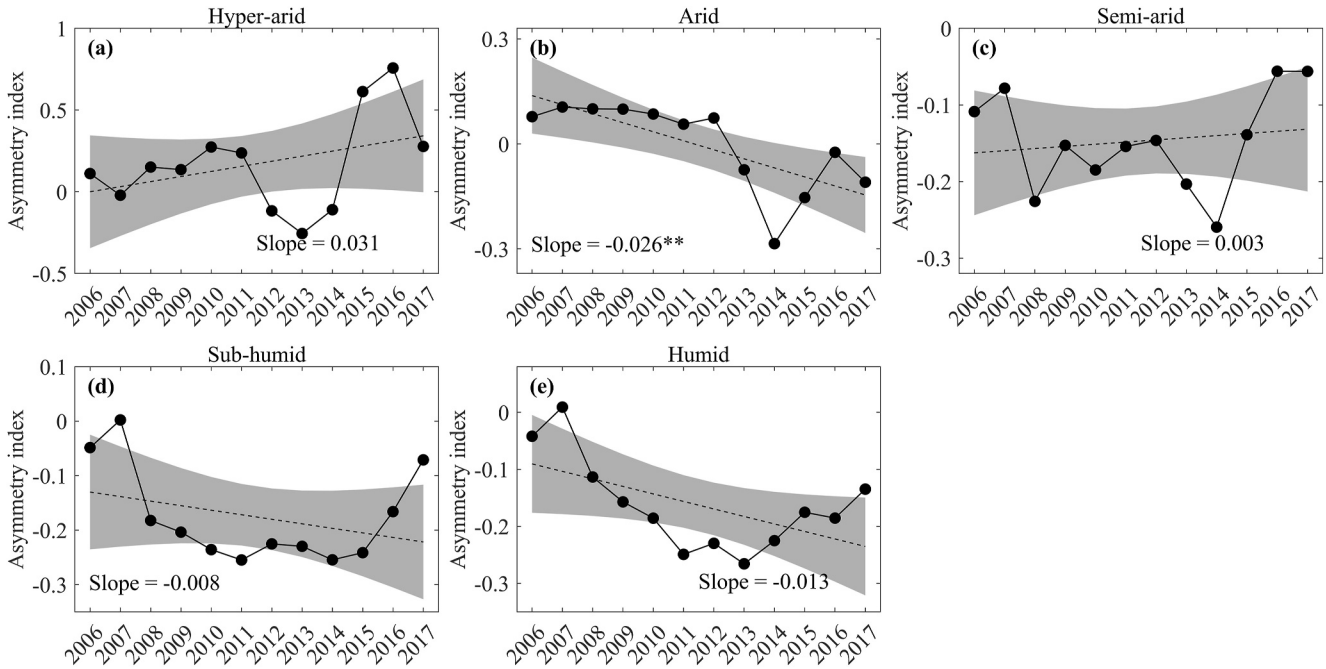

Figure 6. Trends of the tropical GPP asymmetry for each aridity zone during 2001–2022 from GPP_{VPM}, calculated using a 11-year moving window: (a) Hyper-arid regions; (b) Arid regions; (c) Semi-arid regions; (d) Sub-humid regions; (e) Humid regions. The shaded areas represent the 95% confidence interval. * indicates $P < 0.05$ and ** indicates $P < 0.01$.

4.2. Trends of Tropical GPP Asymmetry

We investigated the trends of the GPP asymmetry during 2001–2022 using a 11-year moving window (Figure 5). Spatially, significant increasing trends ($P < 0.1$) in AI_{VPM} were observed for 29.91% of all pixels in the tropics, mainly distributed in southern tropical America, Madagascar, and eastern Australia (Figure 5a). Areas with significantly decreasing trends (covering 32.51% of the tropical regions) were mainly located in tropical rainforests, western Australia, and most parts of tropical Africa (Figure 5a).

Temporally, a significantly decreasing trend of AI_{VPM} was found over the entire pantropical area (Slope = -0.011 years^{-1}, $P < 0.05$, Figure 5b). This could be attributed to the weakened positive GPP response to wet anomalies (Slope of $GPP_W = -0.006$ years^{-1}, $P > 0.05$) and the enhanced negative GPP response (Slope of $GPP_D = -0.006$ years^{-1}, $P < 0.05$) to dry anomalies for the entire pantropical regions (Figure S6a in Supporting Information S1). For the results of GPP_{VPM}, the average AI is negative during 2001–2022 (Figure 5b), and the percentage of negative AI is higher than positive one (Figure 5c), except for the periods centered on the year 2007. Similarly, the decrease of AI values over the study period was also found in GPP_{MODIS} (Slope = -0.01 years^{-1}, $P > 0.05$) (Figure S7 in Supporting Information S1). In addition, we selected multiple window lengths (9, 11, 13, 15 years) to test the robustness of the tropical GPP asymmetry trends, and found that both GPP_{VPM} and GPP_{MODIS} show a decrease in GPP asymmetry across different length windows (Figures S8 and S9 in Supporting Information S1). These results suggest an overall decreasing trend of negative GPP asymmetry in the tropics during 2001–2022.

Interestingly, different trends of AI_{VPM} values were found across aridity zones (Figure 6). During the 2001–2022 period, a decrease in AI_{VPM} values was observed over the arid (Slope = -0.026 years^{-1}, $P < 0.01$, Figure 6b), sub-humid (Slope = -0.008 years^{-1}, $P > 0.05$, Figure 6d) and humid regions (Slope = -0.013 years^{-1}, $P < 0.05$, Figure 6d). Specifically, a decreasing trend of AI_{VPM} in arid regions is mainly attributed to the combination of a weakened positive GPP response to wet anomalies (Slope of $GPP_W = -0.013$ years^{-1}, $P < 0.05$, Figure S6c in Supporting Information S1) and an enhanced negative GPP response (Slope of $GPP_D = -0.013$ years^{-1}, $P < 0.01$, Figure S6c in Supporting Information S1) to dry anomalies. The decrease in AI_{VPM} in sub-humid regions is attributed to the greater enhanced positive GPP response to wet anomalies in comparison to the enhanced negative GPP response to dry anomalies (Figure S6e in Supporting Information S1). For the humid regions, the decrease in

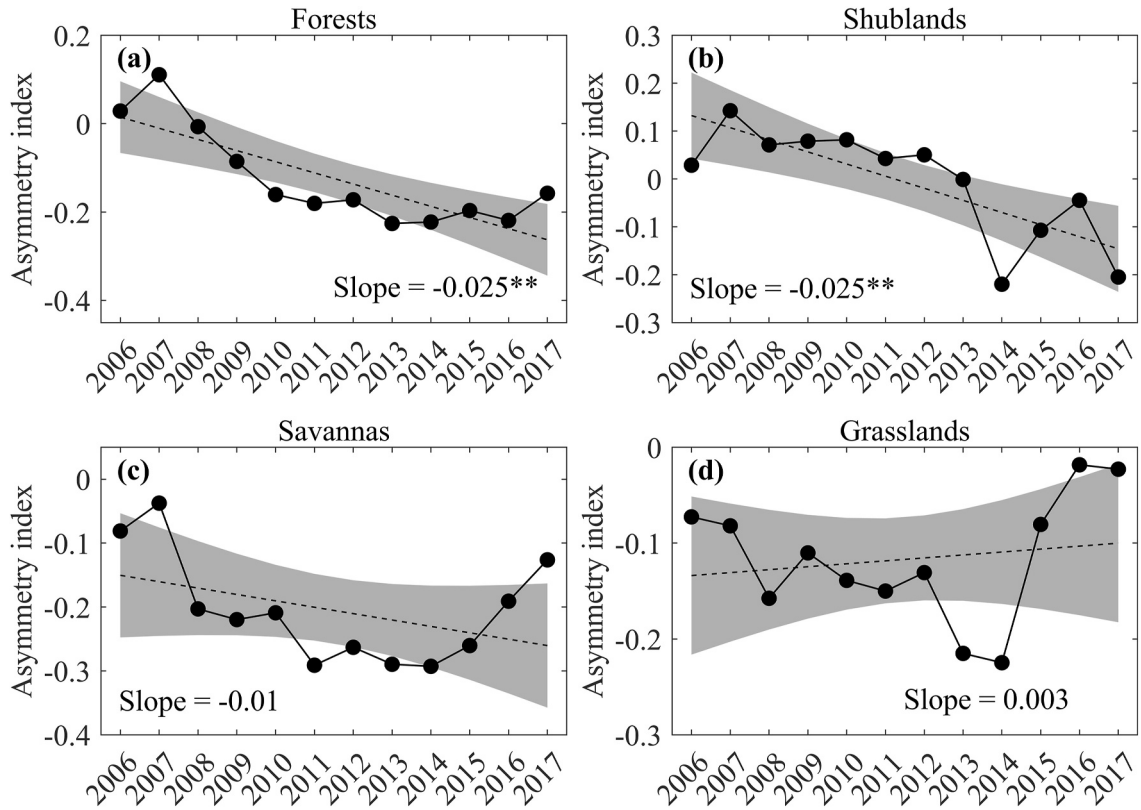

Figure 7. Trends of the tropical GPP asymmetry for different biomes during 2001–2022 from GPP_{VPM}, calculated using a 11-year moving window: (a) Forests; (b) Shrublands; (c) Savannas; (d) Grasslands. The shaded areas represent the 95% confidence interval. * indicates $P < 0.05$ and ** indicates $P < 0.01$.

AI_{VPM} was mainly due to the significant decrease in the positive response of GPP to dry anomalies (Slope of $GPP_D = -0.013$ years^{-1}, $P < 0.01$, Figure S6f in Supporting Information S1). By contrast, an increase in the GPP asymmetry index was observed over the hyper-arid (Slope = 0.031 years^{-1}, $P > 0.05$, Figure 6a) and semi-arid regions (Slope = 0.003 years^{-1}, $P > 0.05$, Figure 6c), which mainly attributed to the enhanced positive GPP response to wet anomalies (Figures S6b and S6d in Supporting Information S1). Similar results were found in AI_{MODIS} (Figure S10 in Supporting Information S1). Thus, the magnitude of decreasing AI_{VPM} over the arid, sub-humid, and humid regions is greater than the magnitude of increasing AI_{VPM} over the hyper-arid and semi-arid regions, leading to an overall decreasing trend of AI_{VPM} over the entire pantropical area.

At the biome level, the AI_{VPM} showed a decreasing trend in forests (Slope = −0.025 years^{-1}, $P < 0.01$, Figure 7a) and shrublands (Slope = −0.025 years^{-1}, $P < 0.01$, Figure 7b). The decreasing trend of AI_{VPM} in forests and shrublands is mainly due to the significant weakening in positive response of GPP to dry anomalies (Slope of $GPP_D = -0.016$ years^{-1}, $P < 0.01$, Figure S11a in Supporting Information S1) and the significant increasing in negative response of GPP to dry anomalies (Slope of $GPP_D = -0.024$ years^{-1}, $P < 0.01$, Figure S11b in Supporting Information S1), respectively. Also, the decrease in AI_{VPM} was found in savannas (Slope = −0.01 years^{-1}, $P > 0.05$, Figure 7c), attributed to the greater weakened positive GPP response to dry anomalies (Slope of $GPP_D = -0.012$ years^{-1}, $P < 0.05$, Figure S11c in Supporting Information S1) in comparison to the weakened negative GPP response to wet anomalies (Slope of $GPP_W = 0.02$ years^{-1}, $P > 0.05$, Figure S11c in Supporting Information S1). Similar results of GPP asymmetry were found in AI_{MODIS}, except for forest biomes (Figure S12 in Supporting Information S1). Conversely, an increase in AI_{VPM} was found in grasslands (Slope = 0.003 years^{-1}, $P > 0.05$, Figure 7d), which is due to the enhanced positive GPP response to wet anomalies (Slope of $GPP_W = 0.001$ years^{-1}, $P > 0.05$, Figure S11d in Supporting Information S1) and weakened negative GPP response to dry anomalies (Slope of $GPP_D = 0.002$ years^{-1}, $P > 0.05$, Figure S11d in Supporting Information S1).

4.3. Influencing Factors on Tropical GPP Asymmetry

We investigated how the mean environmental state of vegetation growth modulated the response of pantropical GPP to precipitation anomalies. The positive asymmetry was observed to decrease with humidity and shift to the negative asymmetry in areas with aridity index > 0.2 (Figure S13a in Supporting Information S1), corresponding to transitional zones between tropical arid and semi-arid regions. Notably, the magnitude of GPP_W and GPP_D values also exhibited a downward trend with increasing aridity index values (Figure S13b in Supporting Information S1), suggesting that GPP responses to precipitation anomalies are stronger in relatively dry regions than in relatively wet regions.

In addition, the positive asymmetry was observed to decrease with precipitation and transition to a negative asymmetry in relatively high precipitation areas (mean annual precipitation >500 mm, Figure S13c in Supporting Information S1), akin to a decreasing trend of AI values along the aridity zone. Similar results were found for RZSM and VPD (Figures S14a and S14d in Supporting Information S1), indicating that the tropical asymmetry correlates with water availability: water-limited regions (i.e., aridity index < 0.2, mean annual precipitation < 500 mm, RZSM < 0.1 m^3 m^{-3}, VPD > 2 kPa) exhibit more positive AI, whereas negative AI predominates in relatively wetter regions.

More pronounced positive AI values are observed along the gradient of radiation, with the positive AI observed in areas with 400 W m^{-2} < PAR < 800 W m^{-2} and 1300 W m^{-2} < PAR < 1400 W m^{-2} (Figure S13e in Supporting Information S1). Meanwhile, GPP showed a positive response to dry anomalies in areas with annual PAR < 1100 W m^{-2}, and this response decreased with increasing PAR (Figure S13f in Supporting Information S1). We then examined the partial correlations of inter-annual variations in GPP with PAR, precipitation and temperature (Figures S15 and S16 in Supporting Information S1), and found that GPP exhibited greater sensitivity to PAR and temperature over tropical humid regions (e.g., tropical rainforests), followed by precipitation. For the tropical drylands (i.e., aridity index < 0.65), changes in GPP are mainly correlated with precipitation as compared to temperature and PAR (Figures S15 and S16 in Supporting Information S1). As a result, increased radiation and temperature during the wet anomalies contribute to the GPP increase in tropical humid regions, leading to the positive GPP_W values, and vice versa for the dry anomalies. Yet, a persistent negative asymmetry was observed along the temperature gradient. Similar results were found for the gradient of soil properties (i.e., SOC and soil sand content) (Figure S17 in Supporting Information S1). Overall, these results indicate that PAR is a strong indicator of both positive and negative GPP asymmetric responses to precipitation anomalies across pantropical regions, especially for the humid regions.

The pantropical GPP asymmetry under different plant physiological and functional traits (i.e., isohydricity, canopy height, and rooting depth) was also explored (Figure 8). GPP asymmetry increased with increasing isohydricity (Figure 8a), indicating that the biomes dominated by anisohydric plant functional traits have a stronger positive asymmetric response to precipitation anomalies than biomes with characterized primarily by isodydric plant functional traits. In addition, biomes with canopy height < 5 m (Figure 8c) or rooting depth > 15 m (Figure 8e) exhibited high positive AI values, suggesting that biomes with shorter canopy height or deeper root length are more prone to exhibiting positive GPP asymmetric responses to precipitation anomalies.

Considering that the tropical asymmetry varied across biomes as well as aridity zones, we further explored the precipitation-GPP relationship during precipitation anomalies for each aridity zone and biome for better understanding the asymmetric response of pantropical GPP to precipitation anomalies. A concave-up curve (i.e., positive asymmetry) for the precipitation-GPP relationship was found over the hyper-arid and arid regions (Figures 9a and 9b). By contrast, a concave-down curve (i.e., negative asymmetry) for the precipitation–GPP relationship was observed over the semi–arid and sub–humid regions (Figures 9c and 9d). In humid regions, a negative precipitation–GPP relationship was observed (Figure 9e), that is, GPP increased with increasing dry anomaly and decreased with increasing wet anomaly.

The precipitation-GPP relationship also varied over tropical drylands (Aridity index < 0.65) and humid areas. A negative precipitation-GPP relationship was found in humid forests and savannas (Figures S18a and S18c in Supporting Information S1), while a concave-down curve for the precipitation-GPP relationship was found in shurblands and dry grasslands (Figures S18b and S18d in Supporting Information S1). No clear precipitation-GPP relationship was observed in dry forests, dry savannas and humid grasslands (Figure S19 in Supporting Information S1).

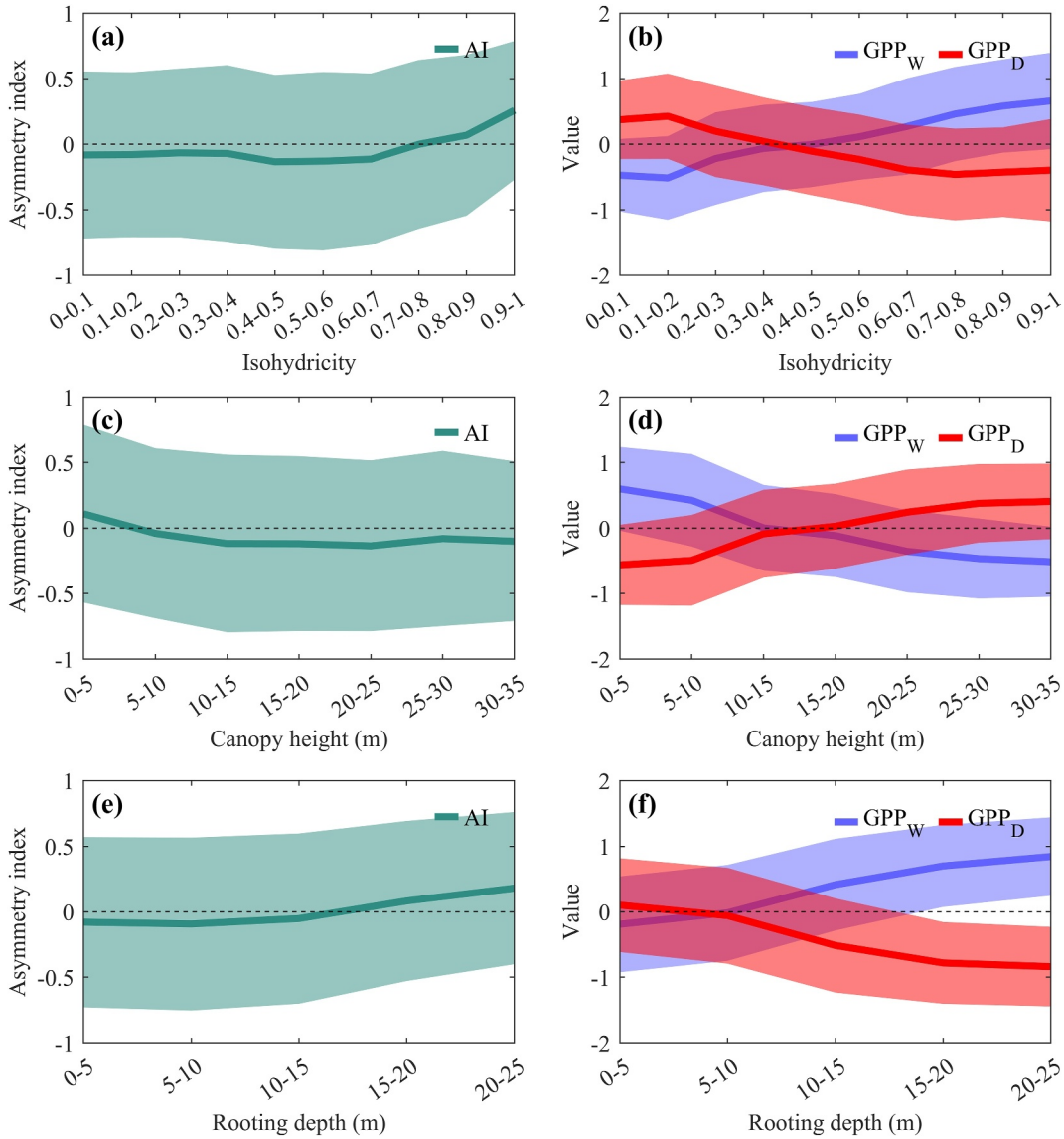

Figure 8. Tropical GPP asymmetry under different plant physiological and functional traits (a, b) Influence of isohydricity on asymmetry index (AI) and GPP_W/GPP_D values, respectively. (c, d) Influence of canopy height on AI and GPP_W/GPP_D values, respectively. (e, f) Influence of rooting depth on AI and GPP_W/GPP_D values, respectively. The green line represents the median AI values, namely, the asymmetric GPP response to precipitation anomalies along the gradient of variables. The blue and red lines represent the median values of GPP_W and GPP_D, respectively, indicating the GPP response to wet and dry anomalies. The shaded areas represent the range of standard deviations.

5. Discussion

5.1. Evidence of Negative GPP Asymmetry in the Tropics

Our results indicated a negative asymmetry of tropical GPP during 2001–2022, indicating that the GPP increases are countered by higher reductions of GPP during precipitation anomalies. Compared with prior studies that emphasized the negative impact of individual climate event (such as 2015–2016 El Niño event) on pantropical ecosystem carbon sink (Wigneron et al., 2020; Yang et al., 2022), our findings highlight a predominance of negative tropical GPP asymmetries, providing additional explanations for the variations of tropical carbon balance within the context of global climate changes. Our estimated tropical GPP asymmetry differs from a previous study (Haverd et al., 2017) reporting a positive asymmetry during 1982–2013, especially in Australia, which was considered as a hotspot of positive GPP asymmetry (Haverd et al., 2017; Li, Kug, et al., 2022; Zscheischler,

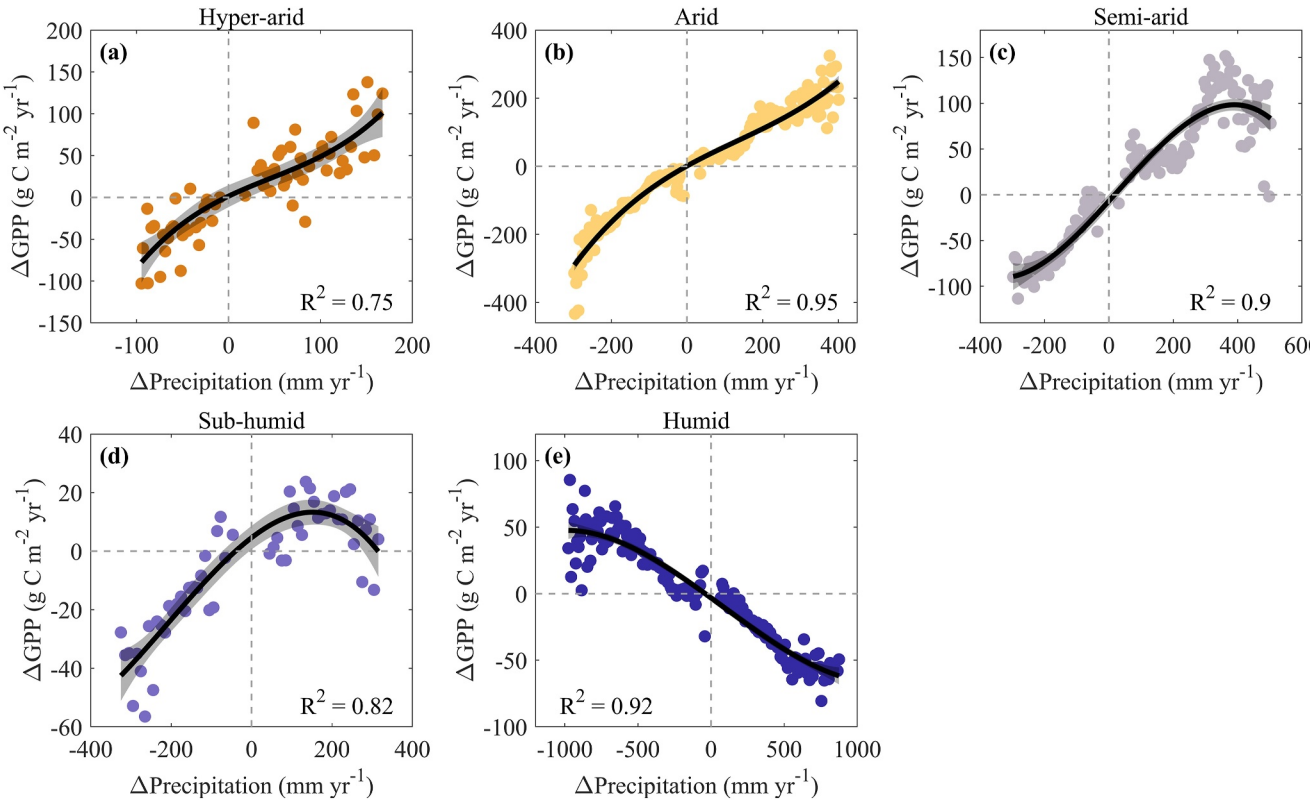

Figure 9. Relationship between Δprecipitation and ΔGPP for each aridity zone: (a) Hyper–arid regions; (b) Arid regions; (c) Semi-arid regions; (d) Sub-humid regions; (e) Humid regions. The *x*-axis (ΔPrecipitation) represents the difference between the average precipitation value during wet/dry years and that during normal precipitation years. The *y*-axis (ΔGPP) represents the difference between the average GPP value during wet/dry years and that during normal precipitation years. The black curves depict the corresponding fitted third-order polynomials, while the shaded areas represent the 95% confidence interval.

Mahecha, et al., 2014). This disparity in GPP asymmetry in Australia could be partly attributed to the increased occurrence of severe droughts, heatwaves, and fires in recent years (Squire et al., 2021), leading to extensive vegetation mortality and large GPP reductions in Australia (Qin et al., 2022).

5.2. Sensitivity of Tropical GPP to Precipitation Anomalies Under Climate Change

Our findings indicated that the sensitivity of tropical GPP to dry anomalies has increased (Slope of $GPP_D < 0$) in drylands over the past two decades, consistent with prior studies (Li, Migliavacca, et al., 2022; Tang et al., 2024; Wei et al., 2023; Zhang et al., 2022). Such long-term variations in the sensitivity of GPP to dry anomalies could be attributed to the elevated atmospheric CO_2 concentrations (Tang et al., 2024; Zhang et al., 2022). Compared to prior studies, our results found a significant decreasing trend of negative asymmetric GPP response to precipitation anomalies in tropics, indicating that the negative impact of inter-annual precipitation variability on tropical vegetation productivity has been intensified. If this negative trend persists, global climate change will have more profound negative impacts on tropical carbon cycle.

A precipitation threshold of 500 mm was found to separate areas of positive asymmetry and negative asymmetry. This observed precipitation threshold found in the tropics is higher than the precipitation thresholds found in mid- to high-latitude Northern Hemisphere (200–400 mm in USA (Al-Yaari et al., 2020) and in China (300–400 mm) (Chang et al., 2023)) as well as at global scale (300 mm) (Gherardi & Sala, 2019; Hou et al., 2021). This suggests that the GPP has a higher sensitivity to precipitation in the tropics than in the Northern Hemisphere. Our results are consistent with previous studies (Chen et al., 2021; Zeng, Hu, et al., 2022) indicating that vegetation productivity remains to be sensitive to precipitation for higher annual rainfall amounts in the tropics compared to in the Northern Hemisphere. This difference observed between the tropics and the Northern Hemisphere could be explained by the high sensitivity of Northern Hemisphere vegetation to temperature (Geng et al., 2022; Piao et al., 2006; Wu et al., 2019).

Note that a negative precipitation-GPP relationship was found in tropical humid forests and savannas, suggesting that the tropical humid biomes may not be suitable for the "double asymmetry" conceptual model (Knapp et al., 2017; Wang et al., 2022). The "double asymmetry" conceptual model suggested an increase or saturation of GPP during wet anomalies and a rapid GPP decrease during dry anomalies (Knapp et al., 2017). Yet, the mechanisms of the asymmetric GPP response to precipitation anomalies varied across different aridity zone. This is because plants can maximize the use of available resources (such as precipitation, solar radiation, temperature, etc.), and adapt to changes in these resources availability (Seastedt & Knapp, 1993). The relative importance of these resources is determined by their quantity in relation to the minimum requirement for vegetation growth (Seastedt & Knapp, 1993), and plants are often more sensitive to the availability of regional limiting resources (Wu et al., 2022). For instance, water availability is the dominant limiting factor in drylands, and vegetation in these regions is more sensitive to the variations of water availability as compared to other resource dynamics (Guo et al., 2015; Huxman, Snyder, et al., 2004). Also, dryland biomes that experienced more frequent occurred water stress tend to be highly drought-tolerant to buffer the GPP reductions during the dry anomalies (Vicente-Serrano et al., 2013; Wang et al., 2022), while high precipitation during wet anomalies can stimulate the rapid growth of dryland biomes and the disproportionate GPP increase (Hsu et al., 2012), leading to a positive asymmetric GPP response to precipitation anomalies in drylands.

On the other hand, in terms of humid biomes (e.g., tropical rainforests), the GPP response to precipitation are constrained by biogeochemical factors (e.g., temperature and radiation), which may be more important for these biomes relative to water availability. For example, during wet anomalies, excessive precipitation in these regions usually becomes runoff that is not available to vegetation, and the limitations of temperature, radiation, and nutrient availability will lead to the reduction of vegetation productivity (Dannenberg et al., 2019). During the dry anomalies, the pulses of radiation and nutrients will facilitate the GPP increases, and the retained soil moisture and the increased water used efficiency may offset the GPP decreases to some extent (Huxman, Smith, et al., 2004; Wang et al., 2022). Meanwhile, given the relatively low sensitivity of vegetation productivity to precipitation in humid regions, tropical humid biomes exhibited a negative precipitation-GPP relationship and a negative asymmetric GPP response to precipitation anomalies. Overall, these mechanisms above could be used to explain the GPP asymmetry in different aridity gradient and how changes in environmental factors during precipitation anomalies affect the tropical GPP asymmetry.

Our findings suggested that biomes dominated by anisohydric plant functional traits showed a stronger positive GPP asymmetry relative to biomes with primarily isohydric plant functional traits, owing to the fact that the anisohydric plants are more drought–tolerant than isohydric plants (Konings & Gentine, 2017; McDowell et al., 2008). Compared to isohydric plants characterized by stomatal closure during drought periods, anisohydric plants can keep their stomata relatively open to maintain photosynthesis (despite being more vulnerable to the xylem embolism) (McDowell et al., 2008), thus exhibiting a strong response of GPP to precipitation anomalies (i.e., biomes characterized primarily by anisohydric plant functional traits have high relative GPP_W/GPP_D values).

Combining the results of the tropical AI along the precipitation gradient and the physiological gradient, we found that the areas with biomes characterized primarily by anisohydric plant functional traits (isohydricity > 0.8) correspond to water-limited areas (mean annual precipitation < 500 mm, aridity index > 0.2), suggesting that the anisohydric biomes more sensitive to the variations of water availability than isohydric biomes. This finding is consistent with a previous study using global remote sensing diurnal observations (Li et al., 2017). In addition, our results of physiological thresholds indicated that taller biomes (canopy height > 5 m) are likely to exhibited isohydric plant functional traits, owing to the fact that taller biomes with strong stomatal regulation can constrain daytime leaf dehydration that cannot be offset by sap replenishment (Konings & Gentine, 2017). Future studies should combine mean climatic and physiological AI thresholds to further investigate the physiological mechanisms of tropical vegetation under water stress.

5.3. Uncertainties

Note that optical remote sensing–based data sets are typically influenced by cloud cover and aerosols during the wet season in tropics (Grogan & Fensholt, 2013; Zeng, Hao, et al., 2022), Zeng, Hu, et al., 2022specially for tropical rainforests. The model-based tropical GPP estimates also suffered from inherent uncertainties of optical remote sensing measurements, rudimentary representation of biogeochemical process, and insufficient ground

observation constrains (Beer et al., 2010; Wang et al., 2024). In addition, all satellite-based GPP data, environmental variables, and ancillary data used in this study were aggregated to a uniform resolution of 0.25°. This approach may introduce uncertainties to our results, especially for tropical rainforests characterized by the greatest species diversity and complex environmental gradients on Earth. For example, multiple biome types (e.g., forests, shrublands, and savannas) may be mixed in a 0.25° pixel, and the dynamics of climate state within that pixel was unified. This potentially leads to a loss of data fidelity and limits our ability to assess the asymmetric GPP response to precipitation anomalies across biomes and arid zones. Besides, only eight EC sites were used in this study, and most of these sites were concentrated in Australia. These factors may potentially cause uncertainties in the evaluation of tropical GPP asymmetry.

For better assessing the uncertainties of tropical GPP asymmetry estimates, we calculated the standard deviation (STD) of AI results across multiple GPP products. Our results showed that the STD values of AI increased with increasing moisture, with the tropical humid regions exhibited the largest STD values (Figure S20 in Supporting Information S1). The relatively large uncertainties of AI estimates within humid regions may be attributed to the varying GPP responses to precipitaiton anomalies across different GPP products, as indicated by the considerable difference in magnitude and direction of GPP_W and GPP_D values among these products (Figures S3 and S4 in Supporting Information S1). Hence, the accuracy of tropical GPP estimates should be improved in the future to better understand the response of tropical carbon cycle to climate changes.

In addition, to test that the asymmetric GPP response calculated in this study (indicated by AI values), we used the same method (see Section 3.1) to calculate the asymmetric response of GPP to temperature and PAR in humid regions (Figure S21 in Supporting Information S1). Our results showed that GPP exhibits a negative asymmetric response to temperature and a positive asymmetric response to PAR. More importantly, significant differences ($P < 0.05$) were observed between the patterns of asymmetric response of GPP to temperature, precipitation, and radiation in tropical humid regions (Figure S21d in Supporting Information S1), indicating that the asymmetric GPP response is mainly related to precipitation.

Indeed, the precipitation, temperature and radiation availability can significantly affect the GPP changes over the tropical humid regions (Beer et al., 2010). Although global evidence suggested that the tropical humid biomes, particularly tropical rainforests, were more sensitive to radiation and temperature than to precipitation (Seddon et al., 2016), the extent of their sensitivity to radiation, temperature and precipitation remains uncertain (Beer et al., 2010; Seddon et al., 2016; Stocker et al., 2019). Thus, it is difficult to define whether precipitation is the dominanting affecting factor on the GPP changes. This means that the asymmetric GPP response calculated in this study was also partly affected by the temperature and radiation. Future study should further explore the mechanism about the asymmetric response of tropical GPP to precipitation anomalies by using vegetation models and field experiments.

Furthermore, the limited period of data availability (2001–2022) constrains the ability to examine the decadal trends of GPP asymmetry over the tropics using a long–term moving window (e.g., a 30-year temporal moving window) and ideally long-term vegetation products should be developed. The calculations of AI values in the present study are based on wet and dry anomalies (Zaveri et al., 2020), without separately considering the effect of individual extreme precipitation event on tropical GPP. In addition, although the asymmetric distribution of precipitation anomalies was still remained, which may introduce uncertainties in this study, we used the multi-year average of standardized precipitation anomalies to reduce the difference in precipitation intensity during wet and dry anomalies. The tropical GPP asymmetry for precipitation extremes should be explored further using vegetation models and field experiments. Several biotic (e.g., vegetation growth potential, biodiversity) and abiotic (e.g., runoff and drainage) factors may also impact tropical GPP asymmetry. Further assessment of these factors is necessary to better evaluate the tropical GPP asymmetry.

6. Conclusions

Using the asymmetry index (AI) across multiple GPP products, our results suggested that tropical GPP overall exhibited a negative asymmetry (AI estimates ranging from −0.115 to −0.041) during 2001–2022, that is, GPP increases over the tropical regions (GPP_W estimates ranging from 0.018 to 0.591) are less than the GPP decreases during precipitation anomalies (GPP_D estimates ranging from −0.694 to −0.099). Most tropical biomes (i.e., forests, savannas, and grasslands) showed negative AI values, with savannas being characterized by the strongest negative AI. Although a positive AI was found in hyper-arid and arid regions, values decreased with

increasing moisture and shifted from being positive to negative. During the period of analysis, a significant decreasing trend of AI was observed over the entire pantropical area, mainly concentrated in arid, sub-humid, and humid regions. Conversely, an increase in AI was found in the hyper-arid and semi-arid regions. At the biome level, a decreasing trend of AI was found in forests, shrublands, and savannas, while an increase in AI was observed in grasslands. Furthermore, the tropical GPP asymmetry is linked to plant physiological and functional strategies for water regulations, with biomes dominated by anisohydric plant functional traits exhibiting higher AI values than biomes with primarily isohydric plant functional traits. Our findings highlight the importance of considering plant functional traits when exploring the asymmetric responses of GPP to precipitation change. Future studies should use multiple auxiliary factors (e.g., CO_2 concentration and nitrogen deposition) and incorporate ecosystem models to further explore the potential mechanisms underlying pantropical GPP asymmetry.

Conflict of Interest

The authors declare no conflicts of interest relevant to this study.

Data Availability Statement

The MODIS land cover map (Friedl et al., 2019) and GPP (Running et al., 2015) are public available from Google Earth Engine (GEE). Also, RZSM, PAR, air temperature from ERA5-land data set (Hersbach, 2019), TerraClimate VPD (Abatzoglou et al., 2018), as well as CHIRPS precipitation (Funk et al., 2015) are publicly available from GEE. The VPM GPP is available through Zhang et al. (2017). The BEPS GPP (Chen et al., 2019), FLUXCOM GPP (Jung et al., 2019), Prentice GPP (Stocker et al., 2020), and BESS GPP (Jiang & Ryu, 2016) are public available. The FLUXNET GPP (Pastorello et al., 2020) and TERN GPP (Karan et al., 2016) are public available. The forest cover loss map and forest degradation map are available through Hansen et al. (2013) and Vancutsem et al. (2021), respectively. The aridity index (Zomer et al., 2022), isohydricity (Li et al., 2017), maximum rooting depth (Fan et al., 2017), and canopy height (Simard et al., 2011) are public available. The SOC and soil sandfraction data can be available from HWSD (Wieder, 2014).

Acknowledgments
This study was funded by the National Natural Science Foundation of China (Grant 42322103, 42171339), the special fund for youth team of Southwest University (SWU-XJLJ202305), the Chongqing Outstanding Youth Science Foundation (CSTB2024NSCQ-JQX0010), and the Chongqing Talents Program (cstc2024ycjh-bgzxm0124).

References

Abatzoglou, J. T., Dobrowski, S. Z., Parks, S. A., & Hegewisch, K. C. (2018). TerraClimate, a high-resolution global dataset of monthly climate and climatic water balance from 1958-2015 [Dataset]. *Scientific Data*, *5*(1), 170191. https://doi.org/10.1038/sdata.2017.191

Ahlstrom, A., Raupach, M. R., Schurgers, G., Smith, B., Arneth, A., Jung, M., et al. (2015). The dominant role of semi-arid ecosystems in the trend and variability of the land CO_2 sink. *Science*, *348*(6237), 895–899. https://doi.org/10.1126/science.aaa1668

Al-Yaari, A., Wigneron, P. J., Ciais, P., Reichstein, M., Ballantyne, A., Ogee, J., et al. (2020). Asymmetric responses of ecosystem productivity to rainfall anomalies vary inversely with mean annual rainfall over the conterminous United States. *Global Change Biology*, *26*(12), 6959–6973. https://doi.org/10.1111/gcb.15345

Beer, C., Reichstein, M., Tomelleri, E., Ciais, P., Jung, M., Carvalhais, N., et al. (2010). Terrestrial gross carbon dioxide uptake: Global distribution and covariation with climate. *Science*, *329*(5993), 834–838. https://doi.org/10.1126/science.1184984

Berg, A., & McColl, K. A. (2021). No projected global drylands expansion under greenhouse warming. *Nature Climate Change*, *11*(4), 331–U371. https://doi.org/10.1038/s41558-021-01007-8

Chang, Q., He, H., Ren, X., Zhang, L., Feng, L., Lv, Y., et al. (2023). Soil moisture drives the spatiotemporal patterns of asymmetry in vegetation productivity responses across China. *Science of the Total Environment*, *855*, 158819. https://doi.org/10.1016/j.scitotenv.2022.158819

Chen, J., Liu, J., Cihlar, J., & Goulden, M. (1999). Daily canopy photosynthesis model through temporal and spatial scaling for remote sensing applications. *Ecological Modelling*, *124*(2), 99–119. https://doi.org/10.1016/S0304-3800(99)00156-8

Chen, J. M., Ju, W., Ciais, P., Viovy, N., Liu, R., Liu, Y., & Lu, X. (2019). Vegetation structural change since 1981 significantly enhanced the terrestrial carbon sink [Dataset]. *Nature Communications*, *10*(1), 4259. https://doi.org/10.1038/s41467-019-12257-8

Chen, M., Rafique, R., Asrar, G. R., Bond-Lamberty, B., Ciais, P., Zhao, F., et al. (2017). Regional contribution to variability and trends of global gross primary productivity. *Environmental Research Letters*, *12*(10), 105005. https://doi.org/10.1088/1748-9326/aa8978

Chen, Z., Liu, H., Xu, C., Wu, X., Liang, B., Cao, J., & Chen, D. (2021). Modeling vegetation greenness and its climate sensitivity with deep-learning technology. *Ecology and Evolution*, *11*(12), 7335–7345. https://doi.org/10.1002/ece3.7564

Dannenberg, M. P., Wise, E. K., & Smith, W. K. (2019). Reduced tree growth in the semiarid United States due to asymmetric responses to intensifying precipitation extremes. *Science Advances*, *5*(10), eaaw0667. https://doi.org/10.1126/sciadv.aaw0667

Espirito-Santo, F. D. B., Gloor, M., Keller, M., Malhi, Y., Saatchi, S., Nelson, B., et al. (2014). Size and frequency of natural forest disturbances and the Amazon forest carbon balance. *Nature Communications*, *5*, 3434. https://doi.org/10.1038/ncomms7638

Famiglietti, C. A., Michalak, A. M., & Konings, A. G. (2021). Extreme wet events as important as extreme dry events in controlling spatial patterns of vegetation greenness anomalies. *Environmental Research Letters*, *16*(7), 074014. https://doi.org/10.1088/1748-9326/abfc78

Fan, L., Dong, G., Frappart, F., Wigneron, J. P., Yue, Y., Xiao, X., et al. (2024). Satellite-observed increase in aboveground carbon over Southwest China during 2013–2021. *Journal of Remote Sensing*, *4*, 0113. https://doi.org/10.34133/remotesensing.0113

Fan, Y., Miguez-Macho, G., Jobbágy, E. G., Jackson, R. B., & Otero-Casal, C. (2017). Hydrologic regulation of plant rooting depth [Dataset]. *Proceedings of the National Academy of Sciences of the United States of America*, *114*(40), 10572–10577. https://doi.org/10.1073/pnas.1712381114

Friedl, M., Sulla-Menashe, D., Tan, B., Schneider, A., Ramankutty, N., Sibley, A., & Huang, X. (2019). MCD12Q1 MODIS/Terra+Aqua land cover type yearly L3 global 500m SIN grid V006 [Dataset]. *NASA EOSDIS Land Processes DAAC*. https://doi.org/10.5067/MODIS/MCD12Q1.006

Funk, C., Peterson, P., Landsfeld, M., Pedreros, D., Verdin, J., Shukla, S., et al. (2015). The climate hazards infrared precipitation with stations--a new environmental record for monitoring extremes [Dataset]. *Scientific Data*, *2*(1), 150066. https://doi.org/10.1038/sdata.2015.66

Geng, X., Zhang, Y., Fu, Y. H., Hao, F., Janssens, I. A., Peñuelas, J., et al. (2022). Contrasting phenology responses to climate warming across the northern extra-tropics. *Fundamental Research*, *2*(5), 708–715. https://doi.org/10.1016/j.fmre.2021.11.035

Gherardi, L. A., & Sala, O. E. (2019). Effect of interannual precipitation variability on dryland productivity: A global synthesis. *Global Change Biology*, *25*(1), 269–276. https://doi.org/10.1111/gcb.14480

González-Zamora, Á., Sánchez, N., Martínez-Fernández, J., & Wagner, W. (2016). Root-zone plant available water estimation using the SMOS-derived soil water index. *Advances in Water Resources*, *96*, 339–353. https://doi.org/10.1016/j.advwatres.2016.08.001

Grogan, K., & Fensholt, R. (2013). Exploring patterns and effects of aerosol quantity flag anomalies in MODIS surface reflectance products in the tropics. *Remote Sensing*, *5*(7), 3495–3515. https://doi.org/10.3390/rs5073495

Guo, Q., Hu, Z., Li, S., Yu, G., Sun, X., Zhang, L., et al. (2015). Contrasting responses of gross primary productivity to precipitation events in a water-limited and a temperature-limited grassland ecosystem. *Agricultural and Forest Meteorology*, *214*, 169–177. https://doi.org/10.1016/j.agrformet.2015.08.251

Hansen, M. C., Potapov, P. V., Moore, R., Hancher, M., Turubanova, S. A., Tyukavina, A., et al. (2013). High-resolution global maps of 21st-century forest cover change [Dataset]. *Science*, *342*(6160), 850–853. https://doi.org/10.1126/science.1244693

Haverd, V., Ahlström, A., Smith, B., & Canadell, J. G. (2017). Carbon cycle responses of semi-arid ecosystems to positive asymmetry in rainfall. *Global Change Biology*, *23*(2), 793–800. https://doi.org/10.1111/gcb.13412

Heinsch, F., Zhao, M., Running, S., Kimball, J., Nemani, R., Davis, K., et al. (2006). Evaluation of remote sensing based terrestrial productivity from MODIS using regional tower eddy flux network observations. *IEEE Transactions on Geoscience and Remote Sensing*, *44*(7), 1908–1925. https://doi.org/10.1109/TGRS.2005.853936

Hersbach, H., Bell, B., Berrisford, P., Biavati, G., Horányi, A., Muñoz Sabater, J., & Thépaut, J. N. (2019). ERA5 monthly averaged data on single levels from 1959 to present [Dataset]. *Copernicus Climate Change Service (C3S) Climate Data Store (CDS)*. https://doi.org/10.24381/cds.f17050d7

Hou, E., Litvak, M. E., Rudgers, J. A., Jiang, L., Collins, S. L., Pockman, W. T., et al. (2021). Divergent responses of primary production to increasing precipitation variability in global drylands. *Global Change Biology*, *27*(20), 5225–5237. https://doi.org/10.1111/gcb.15801

Hsu, J. S., Powell, J., & Adler, P. B. (2012). Sensitivity of mean annual primary production to precipitation. *Global Change Biology*, *18*(7), 2246–2255. https://doi.org/10.1111/j.1365-2486.2012.02687.x

Huxman, T. E., Smith, M. D., Fay, P. A., Knapp, A. K., Shaw, M. R., Loik, M. E., et al. (2004). Convergence across biomes to a common rain-use efficiency. *Nature*, *429*(6992), 651–654. https://doi.org/10.1038/nature02561

Huxman, T. E., Snyder, K. A., Tissue, D., Leffler, A. J., Ogle, K., Pockman, W. T., et al. (2004). Precipitation pulses and carbon fluxes in semiarid and arid ecosystems. *Oecologia*, *141*(2), 254–268. https://doi.org/10.1007/s00442-004-1682-4

Jiang, C., & Ryu, Y. (2016). Multi-scale evaluation of global gross primary productivity and evapotranspiration products derived from Breathing Earth System Simulator (BESS) [Dataset]. *Remote Sensing of Environment*, *186*, 528–547. https://doi.org/10.1016/j.rse.2016.08.030

Jiménez-Muñoz, J. C., Mattar, C., Barichivich, J., Santamaría-Artigas, A., Takahashi, K., Malhi, Y., et al. (2016). Record-breaking warming and extreme drought in the Amazon rainforest during the course of El Nino 2015–2016. *Scientific Reports*, *6*(1), 33130. https://doi.org/10.1038/srep33130

Jung, M., Koirala, S., Weber, U., Ichii, K., Gans, F., Camps-Valls, G., et al. (2019). The FLUXCOM ensemble of global land-atmosphere energy fluxes [Dataset]. *Scientific Data*, *6*(1), 74. https://doi.org/10.1038/s41597-019-0076-8

Jung, M., Schwalm, C., Migliavacca, M., Walther, S., Camps-Valls, G., Koirala, S., et al. (2020). Scaling carbon fluxes from eddy covariance sites to globe: Synthesis and evaluation of the FLUXCOM approach. *Biogeosciences*, *17*(5), 1343–1365. https://doi.org/10.5194/bg-17-1343-2020

Karan, M., Liddell, M., Prober, S. M., Arndt, S., Beringer, J., Boer, M., et al. (2016). The Australian SuperSite network: A continental, long-term terrestrial ecosystem observatory [Dataset]. *Science of the Total Environment*, *568*, 1263–1274. https://doi.org/10.1016/j.scitotenv.2016.05.170

Knapp, A. K., Ciais, P., & Smith, M. D. (2017). Reconciling inconsistencies in precipitation-productivity relationships: Implications for climate change. *New Phytologist*, *214*(1), 41–47. https://doi.org/10.1111/nph.14381

Konings, A. G., & Gentine, P. (2017). Global variations in ecosystem-scale isohydricity. *Global Change Biology*, *23*(2), 891–905. https://doi.org/10.1111/gcb.13389

Li, J., Kug, J. S., Park, S. W., Zhai, P., Huang, M., & Kim, J. S. (2022). Distinct magnitude asymmetries of daily extreme anomalies in gross primary productivity between forests and non-forests. *Climate Dynamics*, *59*(3–4), 767–784. https://doi.org/10.1007/s00382-022-06158-8

Li, W., Migliavacca, M., Forkel, M., Denissen, J. M. C., Reichstein, M., Yang, H., et al. (2022). Widespread increasing vegetation sensitivity to soil moisture. *Nature Communications*, *13*(1), 3959. https://doi.org/10.1038/s41467-022-31667-9

Li, Y., Guan, K., Gentine, P., Konings, A. G., Meinzer, F. C., Kimball, J. S., et al. (2017). Estimating global ecosystem isohydry/anisohydry using active and passive microwave satellite data [Dataset]. *Journal of Geophysical Research-Biogeosciences*, *122*(12), 3306–3321. https://doi.org/10.1002/2017jg003958

Liu, J., Bowman, K. W., Schimel, D. S., Parazoo, N. C., Jiang, Z., Lee, M., et al. (2017). Contrasting carbon cycle responses of the tropical continents to the 2015–2016 El Nino. *Science*, *358*(6360), eaam5690. https://doi.org/10.1126/science.aam5690

Martínez-Fernández, J., Almendra-Martín, L., de Luis, M., González-Zamora, A., & Herrero-Jiménez, C. (2019). Tracking tree growth through satellite soil moisture monitoring: A case study of Pinus Halepensis in Spain. *Remote Sensing of Environment*, *235*, 111422. https://doi.org/10.1016/j.rse.2019.111422

McDowell, N., Pockman, W. T., Allen, C. D., Breshears, D. D., Cobb, N., Kolb, T., et al. (2008). Mechanisms of plant survival and mortality during drought: Why do some plants survive while others succumb to drought? *New Phytologist*, *178*(4), 719–739. https://doi.org/10.1111/j.1469-8137.2008.02436.x

Niu, S., Luo, Y., Li, D., Cao, S., Li, D., Li, J., & Smith, M. D. (2014). Plant growth and mortality under climatic extremes: An overview. *Environmental and Experimental Botany*, *98*, 13–19. https://doi.org/10.1016/j.envexpbot.2013.10.004

Pan, Y., Birdsey, R. A., Fang, J., Houghton, R., Kauppi, P. E., Kurz, W. A., et al. (2011). A large and persistent carbon sink in the world's forests. *Science*, *333*(6045), 988–993. https://doi.org/10.1126/science.1201609

Pastorello, G., Trotta, C., Canfora, E., Chu, H., Christianson, D., Cheah, Y. W., et al. (2020). The FLUXNET2015 dataset and the ONEFlux processing pipeline for eddy covariance data [Dataset]. *Scientific Data*, *7*(1), 225. https://doi.org/10.1038/s41597-020-0534-3

Piao, S., Friedlingstein, P., Ciais, P., Zhou, L., & Chen, A. (2006). Effect of climate and CO_2 changes on the greening of the Northern Hemisphere over the past two decades. *Geophysical Research Letters*, *33*(23), L23402. https://doi.org/10.1029/2006gl028205

Qin, Y., Xiao, X., Wigneron, J. P., Ciais, P., Canadell, J. G., Brandt, M., et al. (2022). Large loss and rapid recovery of vegetation cover and aboveground biomass over forest areas in Australia during 2019–2020. *Remote Sensing of Environment*, *278*, 113087. https://doi.org/10.1016/j.rse.2022.113087

Running, S., Mu, Q., & Zhao, M. (2015). MOD17A2H MODIS/terra gross primary productivity 8-day L4 global 500m SIN grid V006 [Dataset]. *NASA EOSDIS Land Processes Distributed Active Archive Center*. https://doi.org/10.5067/MODIS/MOD17A2H.006

Seastedt, T. R., & Knapp, A. K. (1993). Consequences of nonequilibrium resource availability across multiple time scales: The transient maxima hypothesis. *The American Naturalist*, *141*(4), 621–633. https://doi.org/10.1086/285494

Seddon, A. W. R., Macias-Fauria, M., Long, P. R., Benz, D., & Willis, K. J. (2016). Sensitivity of global terrestrial ecosystems to climate variability. *Nature*, *531*(7593), 229–232. https://doi.org/10.1038/nature16986

Simard, M., Pinto, N., Fisher, J. B., & Baccini, A. (2011). Mapping forest canopy height globally with spaceborne lidar [Dataset]. *Journal of Geophysical Research*, *116*(G4), G04021. https://doi.org/10.1029/2011jg001708

Squire, D. T., Richardson, D., Risbey, J. S., Black, A. S., Kitsios, V., Matear, R. J., et al. (2021). Likelihood of unprecedented drought and fire weather during Australia's 2019 megafires. *Npj Climate and Atmospheric Science*, *4*(1), 64. https://doi.org/10.1038/s41612-021-00220-8

Stocker, B. D., Wang, H., Smith, N. G., Harrison, S. P., Keenan, T. F., Sandoval, D., et al. (2020). P-Model v1.0: An optimality-based light use efficiency model for simulating ecosystem gross primary production [Dataset]. *Geoscientific Model Development*, *13*(3), 1545–1581. https://doi.org/10.5194/gmd-13-1545-2020

Stocker, B. D., Zscheischler, J., Keenan, T. F., Prentice, I. C., Seneviratne, S. I., & Peñuelas, J. (2019). Drought impacts on terrestrial primary production underestimated by satellite monitoring. *Nature Geoscience*, *12*(4), 264–270. https://doi.org/10.1038/s41561-019-0318-6

Sun, J., Zhang, B., Pan, Q., Liu, W., Wang, X., Huang, J., et al. (2023). Nonlinear response of productivity to precipitation extremes in the Inner Mongolia grassland. *Functional Ecology*, *37*(6), 1663–1673. https://doi.org/10.1111/1365-2435.14328

Tang, J., Niu, B., Hu, Z., & Zhang, X. (2024). Increasing susceptibility and shortening response time of vegetation productivity to drought from 2001 to 2021. *Agricultural and Forest Meteorology*, *352*, 110025. https://doi.org/10.1016/j.agrformet.2024.110025

Vancutsem, C., Achard, F., Pekel, J. F., Vieilledent, G., Carboni, S., Simonetti, D., et al. (2021). Long-term (1990–2019) monitoring of forest cover changes in the humid tropics [Dataset]. *Science Advances*, *7*(10). https://doi.org/10.1126/sciadv.abe1603

Vicente-Serrano, S. M., Gouveia, C., Camarero, J. J., Beguería, S., Trigo, R., López-Moreno, J. I., et al. (2013). Response of vegetation to drought time-scales across global land biomes. *Proceedings of the National Academy of Sciences of the United States of America*, *110*(1), 52–57. https://doi.org/10.1073/pnas.1207068110

Wang, T., Zhang, Y., Yue, C., Lyu, G., Wei, J., Yang, H., et al. (2024). Progress and challenges in remotely sensed terrestrial carbon fluxes. *Geo-spatial Information Science*, 1–21. https://doi.org/10.1080/10095020.2024.2336599

Wang, Y., Xiao, J., Li, X., & Niu, S. (2022). Global evidence on the asymmetric response of gross primary productivity to interannual precipitation changes. *Science of the Total Environment*, *814*, 152786. https://doi.org/10.1016/j.scitotenv.2021.152786

Wei, X., He, W., Zhou, Y., Cheng, N., Xiao, J., Bi, W., et al. (2023). Increased sensitivity of global vegetation productivity to drought over the recent three decades. *Journal of Geophysical Research-Atmospheres*, *128*(7), e2022JD037504. https://doi.org/10.1029/2022jd037504

Wieder. (2014). Regridded harmonized World soil database v1.2 [Dataset]. *ORNL Distributed Active Archive Center*. Retrieved from https://daac.ornl.gov/SOILS/guides/HWSD.html

Wigneron, J. P., Ciais, P., Li, X., Brandt, M., Canadell, J. G., Tian, F., et al. (2024). Global carbon balance of the forest: Satellite-based L-VOD results over the last decade. *Frontiers in Remote Sensing*, *5*, 1338618. https://doi.org/10.3389/frsen.2024.1338618

Wigneron, J. P., Fan, L., Ciais, P., Bastos, A., Brandt, M., Chave, J., et al. (2020). Tropical forests did not recover from the strong 2015–2016 El Nino event. *Science Advances*, *6*(6), eaay4603. https://doi.org/10.1126/sciadv.aay4603

Wu, C., Peng, J., Ciais, P., Peñuelas, J., Wang, H., Beguería, S., et al. (2022). Increased drought effects on the phenology of autumn leaf senescence. *Nature Climate Change*, *12*(10), 943–949. https://doi.org/10.1038/s41558-022-01464-9

Wu, X., Guo, W., Liu, H., Li, X., Peng, C., Allen, C. D., et al. (2019). Exposures to temperature beyond threshold disproportionately reduce vegetation growth in the northern hemisphere. *National Science Review*, *6*(4), 786–795. https://doi.org/10.1093/nsr/nwy158

Yang, H., Ciais, P., Wigneron, J. P., Chave, J., Cartus, O., Chen, X., et al. (2022). Climatic and biotic factors influencing regional declines and recovery of tropical forest biomass from the 2015/16 El Nino. *Proceedings of the National Academy of Sciences of the United States of America*, *119*(26). https://doi.org/10.1073/pnas.2101388119

Yue, C., Ciais, P., Bastos, A., Chevallier, F., Yin, Y., Rödenbeck, C., & Park, T. (2017). Vegetation greenness and land carbon-flux anomalies associated with climate variations: A focus on the year 2015. *Atmospheric Chemistry and Physics*, *17*(22), 13903–13919. https://doi.org/10.5194/acp-17-13903-2017

Zaveri, E., Russ, J., & Damania, R. (2020). Rainfall anomalies are a significant driver of cropland expansion. *Proceedings of the National Academy of Sciences of the United States of America*, *117*(19), 10225–10233. https://doi.org/10.1073/pnas.1910719117

Zeng, X., Hu, Z., Chen, A., Yuan, W., Hou, G., Han, D., et al. (2022). The global decline in the sensitivity of vegetation productivity to precipitation from 2001 to 2018. *Global Change Biology*, *28*(22), 6823–6833. https://doi.org/10.1111/gcb.16403

Zeng, Y., Hao, D., Huete, A., Dechant, B., Berry, J., Joiner, J., et al. (2022). Optical vegetation indices for monitoring terrestrial ecosystems globally. *Nature Reviews Earth & Environment*, *3*(7), 477–493. https://doi.org/10.1038/s43017-022-00298-5

Zhang, Y., Gentine, P., Luo, X., Lian, X., Liu, Y., Zhou, S., et al. (2022). Increasing sensitivity of dryland vegetation greenness to precipitation due to rising atmospheric CO_2. *Nature Communications*, *13*(1), 4875. https://doi.org/10.1038/s41467-022-32631-3

Zhang, Y., Xiao, X., Wu, X., Zhou, S., Zhang, G., Qin, Y., & Dong, J. (2017). A global moderate resolution dataset of gross primary production of vegetation for 2000-2016 [Dataset]. *Scientific Data*, *4*(1), 170165. https://doi.org/10.1038/sdata.2017.165

Zhao, H., Jia, G., Xu, X., & Zhang, A. (2022). Contrasting responses of vegetation production to rainfall anomalies across the northeast China transect. *Journal of Geophysical Research-Biogeosciences*, *127*(6). https://doi.org/10.1029/2022jg006842

Zomer, R. J., Xu, J., & Trabucco, A. (2022). Version 3 of the global aridity index and potential evapotranspiration database [Dataset]. *Scientific Data*, *9*(1), 409. https://doi.org/10.1038/s41597-022-01493-1

Zscheischler, J., Mahecha, M. D., von Buttlar, J., Harmeling, S., Jung, M., Rammig, A., et al. (2014). A few extreme events dominate global interannual variability in gross primary production. *Environmental Research Letters*, *9*(3), 035001. https://doi.org/10.1088/1748-9326/9/3/035001

Zscheischler, J., Reichstein, M., Harmeling, S., Rammig, A., Tomelleri, E., & Mahecha, M. D. (2014). Extreme events in gross primary production: A characterization across continents. *Biogeosciences*, *11*(11), 2909–2924. https://doi.org/10.5194/bg-11-2909-2014